ACS Biomaterials SCIENCE & ENGINEERING
Article
Cite This: ACS Biomater. Sci. Eng. 2019, 5, 5392−5411
pubs.acs.org/journal/abseba

Irregular Load Adapted Scaffold Optimization: A Computational Framework Based on Mechanobiological Criteria

Óscar L. Rodríguez-Montaño,[†,‡] Carlos Julio Cortés-Rodríguez,[†] Francesco Naddeo,[§] Antonio E. Uva,[‡] Michele Fiorentino,[‡] Alessandro Naddeo,[§] Nicola Cappetti,[§] Michele Gattullo,[‡] Giuseppe Monno,[‡] and Antonio Boccaccio*[,‡]

[†]Departamento de Ingeniería Mecánica y Mecatrónica, Universidad Nacional de Colombia, Carrera 30 No. 45-03, Bogotá D.C., Colombia

[‡]Dipartimento di Meccanica, Matematica e Management, Politecnico di Bari, Viale Japigia, 182, 70126 Bari, Italy

[§]Dipartimento di Ingegneria Industriale, Università di Salerno, via Giovanni Paolo II, 132, 84084 Fisciano, SA, Italy

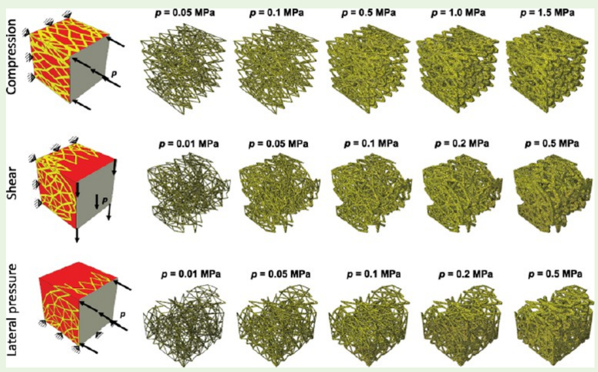

ABSTRACT: By combining load adaptive algorithms with mechanobiological algorithms, a computational framework was developed to design and optimize the microarchitecture of irregular load adapted scaffolds for bone tissue engineering. Skeletonized cancellous bone-inspired lattice structures were built including linear fibers oriented along the internal flux of forces induced by the hypothesized boundary conditions. These structures were then converted into solid finite element models, which were optimized with mechanobiology-based optimization algorithms. The design variable was the diameter of the beams included in the scaffold, while the design objective was the maximization of the fraction of the scaffold volume predicted to be occupied by neo-formed bony tissue. The performance of the designed irregular scaffolds, intended as the capability to favor the formation of bone, was compared with that of the regular ones based on different unit cell geometries. Three different boundary and loading conditions were hypothesized, and for all of them, it was found that the irregular load adapted scaffolds perform better than the regular ones. Interestingly, the numerical predictions of the proposed framework are consistent with the results of experimental studies reported in the literature. The proposed framework appears to be a powerful tool that can be utilized to design high-performance irregular load adapted scaffolds capable of bearing complex load distributions.

KEYWORDS: *load adaptive algorithms, mechanobiological algorithms, irregular and regular scaffolds, robustness of optimized structures, finite element method, structural optimization algorithms*

1. INTRODUCTION

One of the most promising strategies to repair large-dimension bone defects consists in using scaffolds for bone tissue engineering.[1] Scaffolds are porous biomaterials imitating the properties of natural bone that provide a specific environment and architecture for bone growth and development.[2] A number of research studies have been carried out that, based on different criteria,[3−6] aim at maximizing the scaffold performance, i.e., the attitude to promote and favor the tissue regeneration. It is commonly known that the scaffold ability to stimulate the formation of new bony tissue depends on a very large number of factors, among which, as demonstrated by recent in vitro and in vivo studies,[7−9] the scaffold design occupies a prominent place.

Due to the costly and time-expensive protocols typically adopted in experimental bone tissue engineering, in silico models are recently gaining interest. Many computational models are currently being developed to design and optimize the scaffold microarchitecture that allows maximizing the scaffold performance.[4,10,11] Some of these models incorporate mechanobiological (MB) algorithms that investigate the role of biophysical stimuli in the regulation of the tissue differentiation process in bone tissue scaffolds.[3,12−17] Changing the scaffold microarchitecture leads to change the biophysical stimulus acting on the regenerating tissue. The objective of computational mechanobiology-based models is, hence, the identification and the design of the scaffold geometry that yields the most favorable biophysical stimuli, i.e., those that favor the formation of the largest amounts of bone in the shortest time.[18−20]

Two main scaffold geometries can be obtained with the manufacturing technologies currently available: regular and irregular. The first one can be obtained as the replication in the three-dimensional (3D) space of a unit cell geometry; the second one includes, instead, differently shaped and dimensioned pores that generate an irregular microarchitecture. A

Received: July 9, 2019
Accepted: August 22, 2019
Published: August 22, 2019

DOI: 10.1021/acsbiomaterials.9b01023
ACS Biomater. Sci. Eng. 2019, 5, 5392−5411

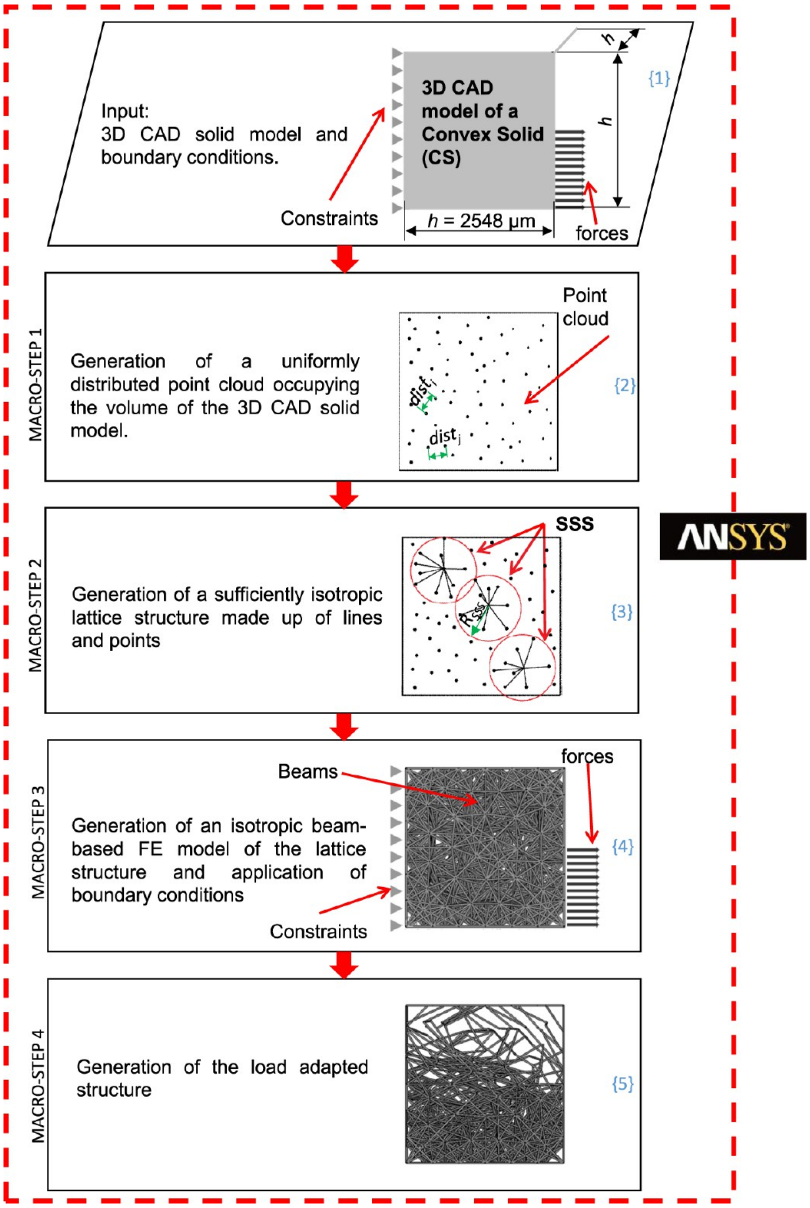

Figure 1. Schematic of the algorithm implemented in Ansys to generate the skeletonized load adapted structure successively dressed and optimized.

number of studies were carried out on regular scaffolds.[21−23] Analytical relationships were also developed to relate the scaffold repeating unit cell geometry with the global equivalent mechanical properties.[24] By implementing mechanobiological (MB) algorithms, the present authors optimized the geometry of regular scaffolds based on different unit cell geometries with both homogeneous[18,25,26] and functionally graded porosity.[27] Regular scaffolds are fabricated with rapid prototyping techniques that allow controlling with high accuracy the dimensions of the single unit cell geometry.[2] However, regular scaffolds are not suited to properly bear complex load distributions that can be supported, more efficiently, by irregular load adapted scaffolds.[28−30] Conventional techniques, such as solvent casting and particle leaching, freeze drying, gas foaming, etc., are utilized to fabricate, using subtractive methods, irregular geometry scaffolds. The main drawback of these techniques is the limited ability to control shapes and geometries. Most of them allow controlling the average dimensions of the scaffold microarchitecture but not the specific dimensions of the single scaffold pore.[2] Extensive studies were carried out to characterize the properties of irregular scaffolds[31−35] and to optimize their performance.[36−41] Computational models were also proposed[42,43] to determine the optimal geometry of irregular scaffolds. However, to date, no studies are reported in the literature that optimize the irregular scaffold geometry on the basis of mechanobiological criteria.

Trabecular bone tissue, i.e., the typical tissue that scaffolds have to replace, is not regular and presents a highly organized structure[44] with trabeculae oriented according to the principal stress directions.[45] Bio-inspired structured materials were recently proposed[46] as well as bio-inspired design techniques were investigated to mimic natural structures.[30] A recent study has demonstrated the capability of bioinspired load adapted structures to adequately bear different boundary and loading conditions.[28] A load adaptive (LA) algorithm was developed replacing the continuous mass of convex solids with a cancellous bone-inspired lattice structure organized to have linear fibers oriented according to the boundary conditions.

DOI: 10.1021/acsbiomaterials.9b01023
ACS Biomater. Sci. Eng. 2019, 5, 5392−5411

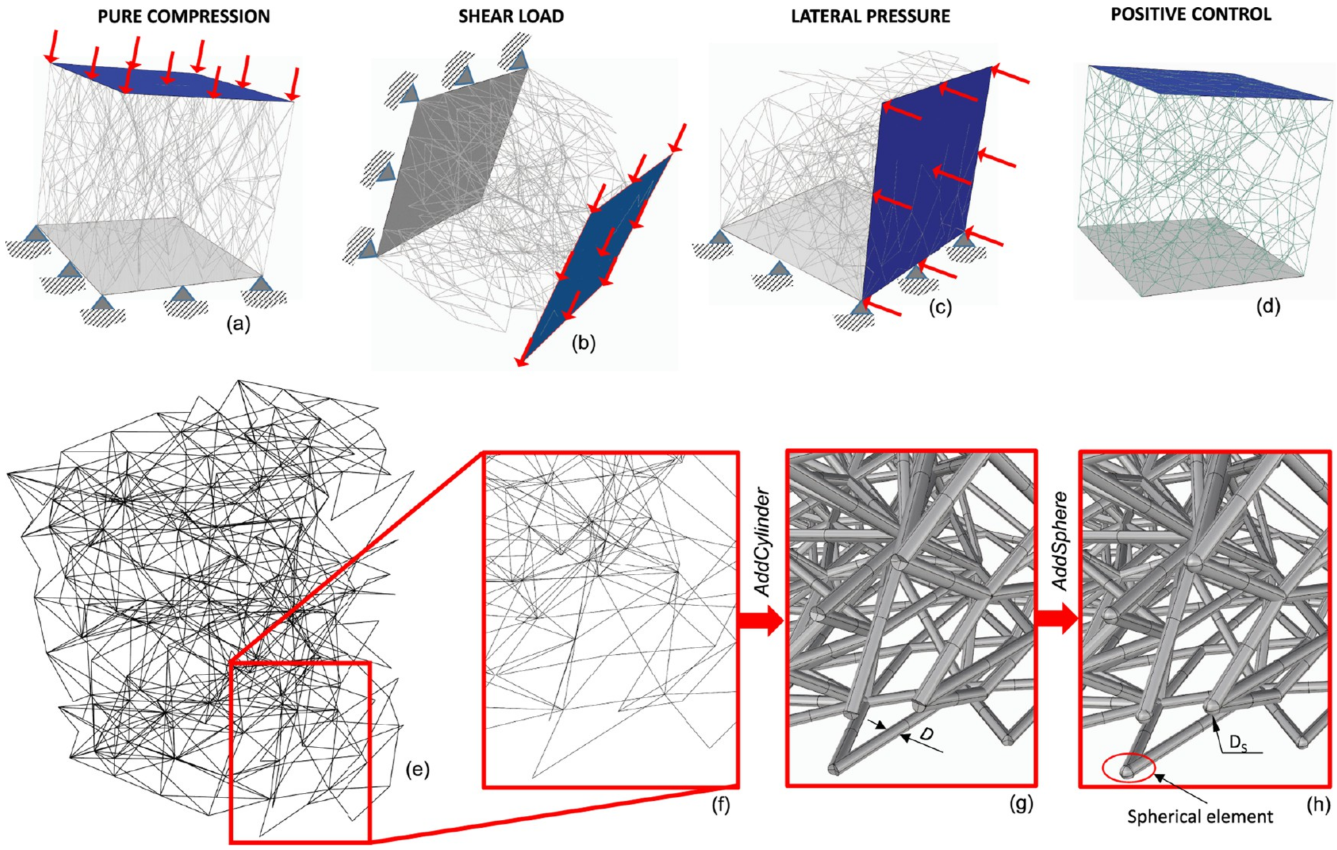

Figure 2. Skeletonized load adapted structures generated in the Ansys environment for different boundary and loading conditions: pure compression (a), shear load (b), and lateral pressure (c). The structures were imported into Rhinoceros (e, f) where cylinders (g) were built around each line segment and spherical elements (h) were added in the proximity of each convergence node. For the sake of brevity, the CAD operations performed with Rhinoceros are shown only for the structure subjected to lateral pressure (c). To evaluate the efficiency of the proposed LA algorithm, a structure was built (d) including randomly oriented beams, which was used as the positive control and which was subjected to all of the three hypothesized boundary and loading conditions.

The aim of this study was to propose a computational framework that combines MB and LA algorithms to design and optimize the geometry of irregular load adapted scaffolds. In other words, a mechanobiology-based optimization algorithm was integrated with a load adaptive algorithm to determine the optimal geometry of irregular load adapted scaffolds. Three different boundary and loading conditions were hypothesized originating simple and complex load distributions. Comparisons were finally made between the mechanobiological performances, quantified as the percentage of the total scaffold volume occupied by neo-formed bony tissue, of irregular and regular scaffolds. Interestingly, we found that in all of the hypothesized boundary and loading conditions, irregular load adapted scaffolds allow including, within the pores, larger amounts of bone, compared to the regular ones. In addition, we found that the irregular load adapted scaffolds are also more robust than the regular ones. In other words, they display a more suited structural response in the case when they are subjected to boundary and loading conditions slightly different with respect to those for which they were optimized. To corroborate the proposed framework, comparisons were made between the numerical predictions and the experimental observations of in vivo studies. Interestingly, the numerical predictions are consistent with the experimental findings. The proposed framework appears a powerful tool to design high-performance irregular load adapted scaffolds. Compared to the regular ones, these scaffolds have the potentialities to include larger amounts of bone and hence to increase the success rate of the scaffold implantation procedure.

2. MATERIALS AND METHODS

2.1. Computational Framework. The proposed computational framework is articulated into two principal parts. The first part includes load adaptive algorithms and serves to generate the base wireframe structure of the scaffold. In this first part, optimization processes are implemented, aimed to identify the beams of the scaffold that are actually useful to bear the load. The resulting skeletonized structures are successively "dressed", made three-dimensional structures, and given as input to the second part of the computational framework. This second part implements computational mechanobiological models and aims to optimize the dimension of the diameter of beams. Further details on the framework are given in the following sections.

2.2. Generation of Irregular Load Adapted Structures. The load adaptive (LA) algorithm, which consists of a single source code written in Ansys Parametric Design Language (APDL) of commercial software Ansys (Release 16.2, ANSYS, Inc., Canonsburg, Pennsylvania), generates the base wireframe structure of the scaffold, i.e., the scaffold skeleton that will be successively dressed and made a solid three-dimensional structure. In detail, the LA algorithm replaces the solid mass of a convex solid (CS) of any shape subjected to static loads with a lattice structure having the beams oriented along the internal flux of forces induced by the hypothesized boundary conditions. The algorithm takes in input both the 3D computer-aided design (CAD) model of CS and the boundary conditions in the form of forces and/or displacements (Figure 1, block {1}) and gives in output the lattice structure with beams properly oriented and inscribed within the volume

DOI: 10.1021/acsbiomaterials.9b01023
ACS Biomater. Sci. Eng. 2019, 5, 5392−5411

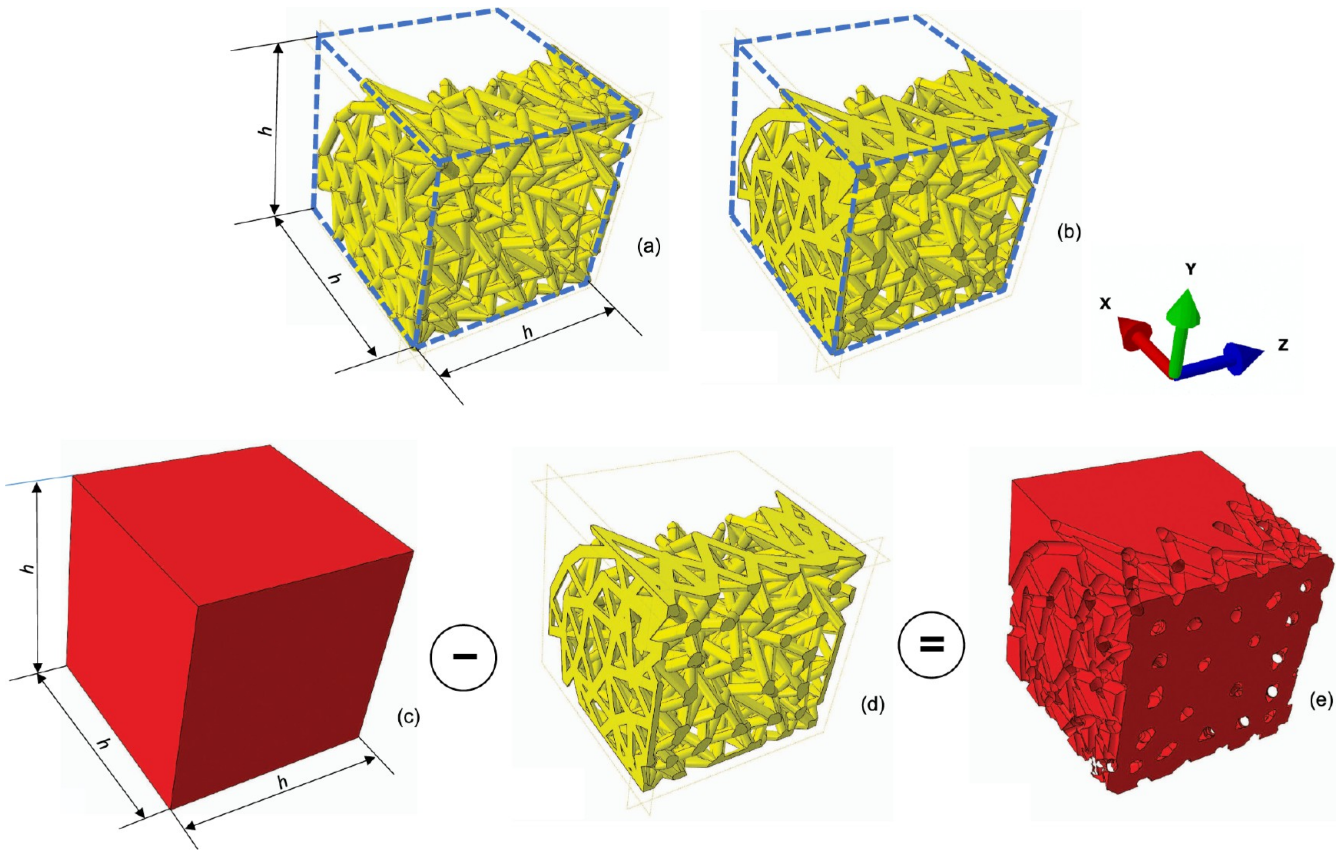

Figure 3. Scaffold model imported into Abaqus (a) was cut along the faces of the cubic volume with the side h (b). The model of the granulation tissue (e) was obtained via the boolean operation of subtraction, from the cubic volume $h \times h \times h$ (c), the volume of the cut scaffold (d).

Table 1. Values of Material Properties Implemented in the Models of Scaffold and Granulation Tissue

material properties	scaffold	granulation tissue
Young's modulus [MPa]	1000	0.2
Poisson's ratio	0.3	0.167
permeability [$m^4/(N\ s)$]	1×10^{-14}	1×10^{-14}
porosity	0.5	0.8
bulk modulus grain [MPa]	13 920	2300
bulk modulus fluid [MPa]	2300	2300

of the CS model. Following a previous study,[25] a cubic volume of side h = 2548 μm was considered as a CS model (Figure 1, block {1}).

The first macrostep is the generation of a uniformly distributed point cloud occupying the volume of the cubic 3D CAD solid model showing the identical distribution of points on the opposite sides (Figure 1, block {2}). Then, the algorithm generates a sufficiently isotropic finite element (FE) lattice structure made up of beams (second macrostep, Figure 1, block {3}). To do this, the following substeps are followed:

- For each generated point of the point cloud, a spherical space of selection (SSS) is defined that includes a specified number of points.
- Line segments are generated that join the center of SSS with each point included in SSS. The average number of beams (ANB) departing from each converging nodes can be specified by the user.
- The line segments are converted into beams, and a sufficiently isotropic beam-based finite element (FE) model of the lattice structure is generated by means of an ad hoc written isotropic criterion that uses periodic boundary conditions taking advantage of the identical distribution of nodes on opposite sides.[47]

Then, the third macrostep follows (Figure 1, block {4}). An FE lattice structure is generated including only the beams more significantly loaded under the hypothesized boundary conditions. This macrostep is articulated in the following substeps:

- The boundary conditions are applied.
- An optimization process starts: the elastic solution is iteratively calculated, and the beams less stressed are deleted until the number of beams converging in each convergence node becomes equal to the a priori fixed parameter ANB. It is possible to set the number of beams to be removed (Δ_b) at each cycle after convergence analysis of the results in terms of mechanical performance and computational weight. In all of these iterative FE analyses, the structural continuity is constantly preserved. Further details on the LA algorithm are reported in a previous study.[28]

It is worth noting that the load adaptive algorithm does not require to define a specific load value because it is based on the relative comparison between the stress states acting on the beams. In general, the algorithm calculates iteratively the elastic solution and deletes the beams less stressed. The threshold level of stress under which the beam must be removed is a function of the load; the higher the load, the larger the threshold level of stress. As a consequence of this, the beams that are deleted by the load adaptive algorithm will always be the same independent of the specific value of load acting on the skeletonized structure.

A load adapted skeletonized structure is finally generated (Figure 1, block {5}, fourth macrostep), which includes line segments oriented along the internal flux of forces induced by the boundary conditions.

The algorithm requires the user to set the values of three input parameters: (i) the average number of beams (ANB); (ii) the average distance dist between the points of the cloud generated in the first macrostep; and (iii) the radius R_{SSS} of the spherical spaces of selection (Figure 1). Following Lakatos et al.,[48] the average number of beams,

DOI: 10.1021/acsbiomaterials.9b01023
ACS Biomater. Sci. Eng. 2019, 5, 5392−5411

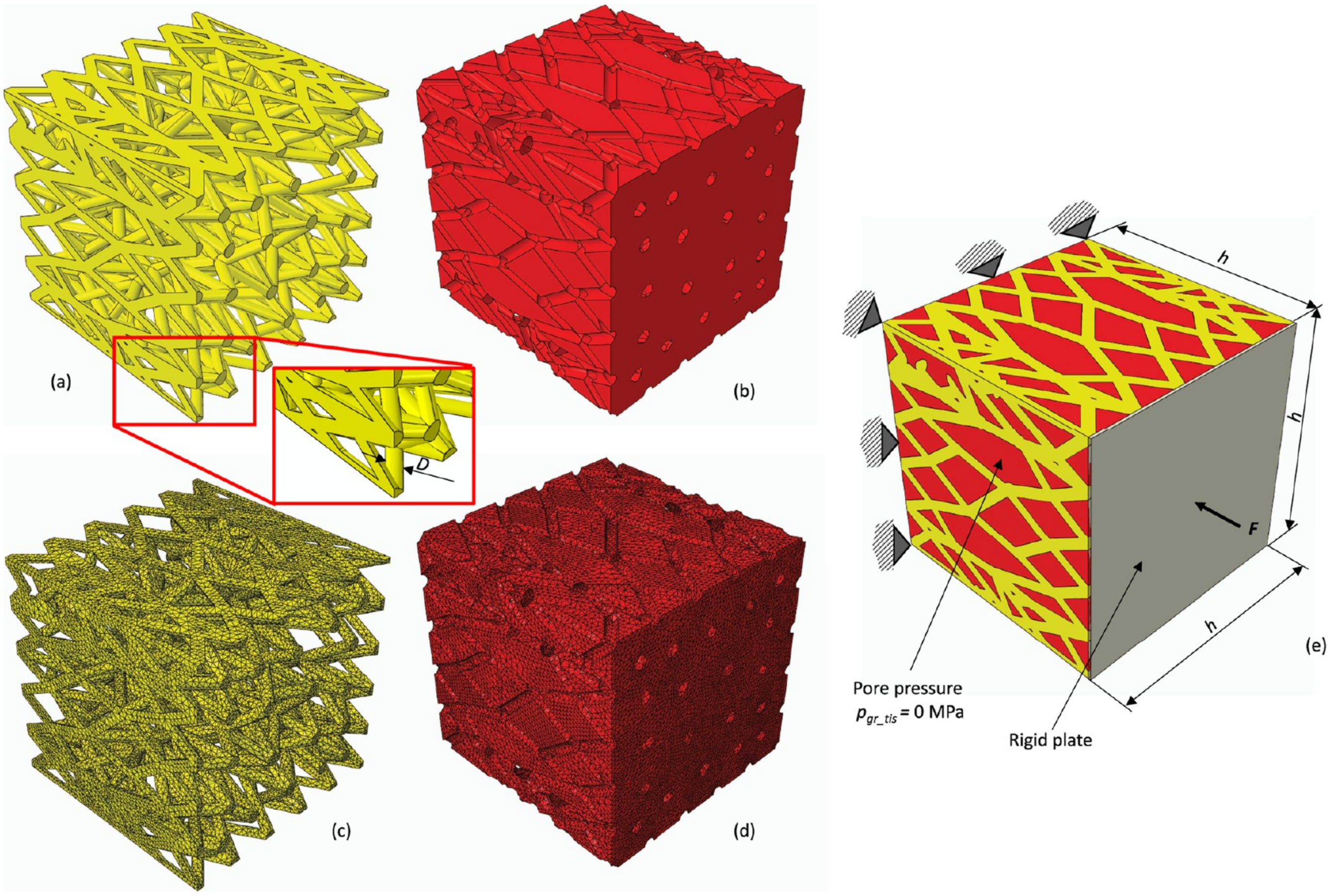

Figure 4. Models of scaffold (a) and granulation tissue (b) obtained from the (skeletonized) structure adapted to pure compression load were meshed with tetrahedral elements (c, d), assembled and subjected to boundary and loading conditions (e). All of the cylindrical elements had the same diameter D (a).

ANB, was set equal to 6, which is the average number of trabeculae converging in "nodes" of the human cancellous bone. The distance dist and the radius R_{SSS} were set equal to dist = $h/5$ and R_{SSS} = 1.7 × dist = 1.7 × $h/5$ = 0.34 × h, which allow building line segments with an average length consistent with that of trabeculae of the human cancellous bone.[48−50]

Three different boundary and loading conditions were hypothesized: (i) a pure compression, where the convergence nodes of the bottom surface were clamped, while those of the upper surface were subjected to a distributed compression load (Figure 2a); (ii) a shear load, where the convergence nodes of the bottom surface were constrained as in the previous case, while those of the upper surface were subjected to a distributed shear load (Figure 2b); and (iii) a lateral pressure, where the convergence nodes of the bottom surface were clamped and those of the lateral surface were subjected to a distributed compression load (Figure 2c). For each of the hypothesized boundary and loading conditions, one skeletonized structure was generated with the LA algorithm (Figure 2a−c). To evaluate the effect of the LA algorithm, a skeletonized structure was also generated with beams randomly oriented in the space that was used as the positive control (Figure 2d).

2.3. Generation of 3D CAD Scaffold Models. The four skeletonized structures were dressed and made 3D CAD solid models via the 3D computer graphics and computer-aided design (CAD) application software Rhinoceros (version 5, McNeel). The coordinates of the convergence nodes and the connectivity of the line segments were saved in a text file that was given in input to Rhinoceros. By using the CAD tool "AddCylinder", cylindrical elements all with the same diameter D were built having each, as axis, the line segments generated by the load adaptive algorithm (Figure 2e−h). To guarantee the continuity of the structure, spherical elements with a diameter D_S = 1.1 × D were included in the model in correspondence of each convergence node (Figure 2h), via the "AddSphere" CAD tool available in Rhinoceros. Spherical elements with the same dimensions were utilized in a previous study[26] to connect the beams of scaffolds based on the diamond unit cell. The diameter D was the design parameter optimized through the mechanobiology-based algorithm described below. The generated 3D CAD solid model of the scaffold was finally saved in *.sat format and given in input to Abaqus, where the 3D finite element model of the scaffold was built. To make the procedure easily incorporable in an algorithm, a python script was written that, given in input to Rhinoceros, allows all of the CAD operations described above to be executed automatically.

2.4. Generation of 3D Finite Element Models of Scaffold. The four CAD models in *.sat format generated by Rhinoceros were then imported into Abaqus (version 6.12, Dassault Systèmes, France), where they were cut along the faces of the cubic volume of side h (Figure 3a,b). The model of the granulation tissue occupying the scaffold pores was then obtained with the Boolean operation of subtraction, from the cubic volume V_{cube} = $h \times h \times h$, the volume of the scaffold (Figure 3c−e). Both the scaffold and the granulation tissue were modeled as biphasic poroelastic materials; the material properties implemented in the models were taken from previous studies[25,26] and are listed in Table 1.

The solid models of scaffold and granulation tissue generated for the hypothesized boundary and loading conditions (i.e., pure compression (Figure 4), shear load (Figure 5), lateral pressure (Figure 6), model with randomly oriented beams (control) (Figure 7)) were discretized into tetrahedral four-node, linear displacement, and pore pressure elements (C3D4P) available in Abaqus. The average element size was set equal to 50 μm, while the maximum deviation factor for the curvature control was fixed to 0.01 (Figures 4c,d, 5c,d, 6c,d, and 7c,d). The sophisticated geometry of scaffold and granulation tissue models, the presence of geometric "impurities" such as very small faces and

DOI: 10.1021/acsbiomaterials.9b01023
ACS Biomater. Sci. Eng. 2019, 5, 5392−5411

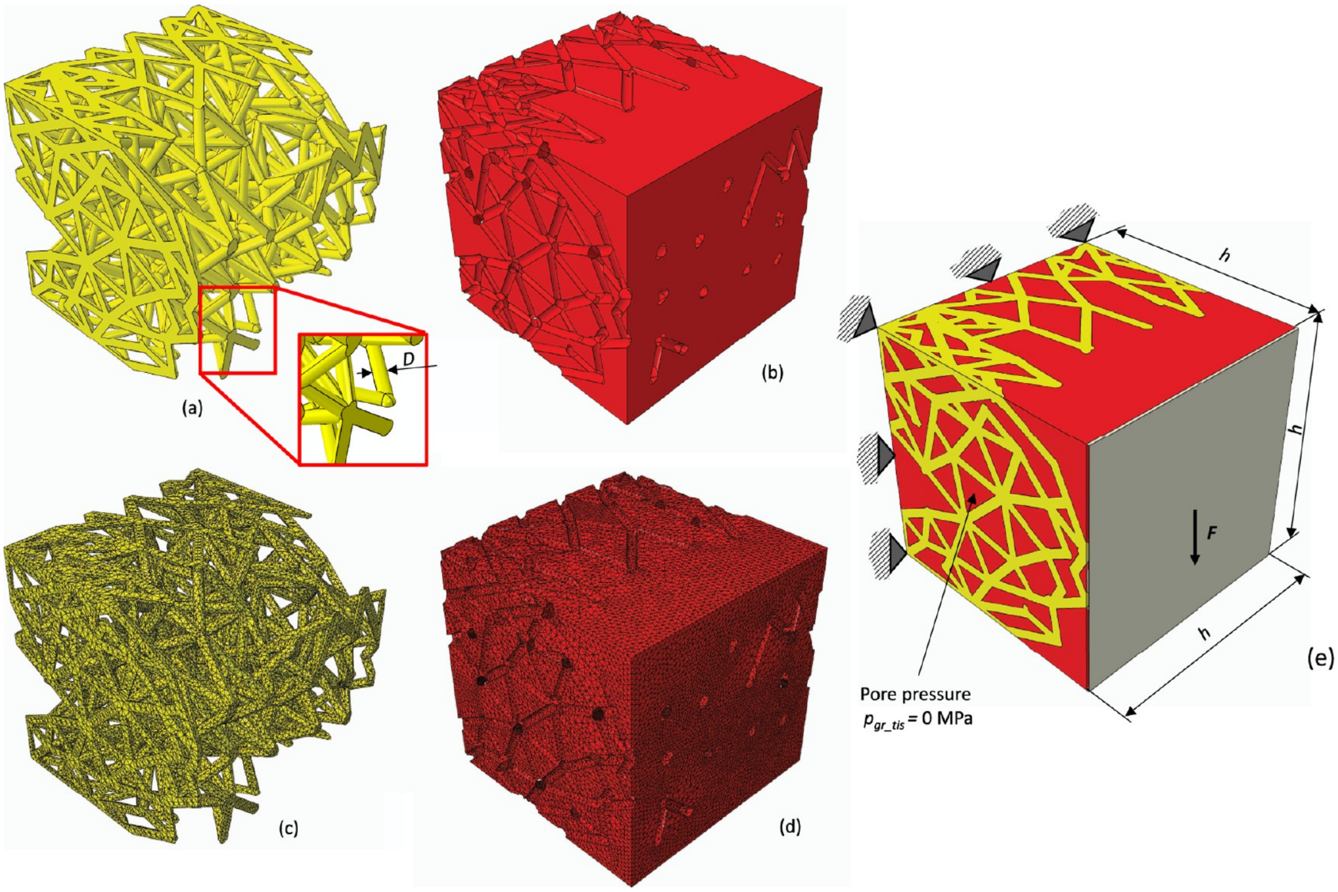

Figure 5. Models of scaffold (a) and granulation tissue (b) obtained from the structure adapted to shear load were meshed with tetrahedral elements (c, d), assembled and subjected to boundary and loading conditions (e). All of the cylindrical elements had the same diameter *D* (a).

edges generated in the previous CAD operations, made the meshing process tremendously difficult and, very often, unsuccessful. To address this issue, the virtual topology toolset available in Abaqus was utilized that allows removing small details by combining a small face with an adjacent face or by combining a small edge with an adjacent edge.

A "tie" constraint was utilized to tie the adjacent surfaces of scaffold and granulation tissue so as to remove any relative motion between them. The bottom surface of the scaffold/granulation tissue model was clamped, while equation constraints were utilized to fix a rigid plate to one of the faces of the model. In detail, in the case of the pure compression (Figure 4) and shear load (Figure 5), the rigid plate was fixed on the top surface; in the case of the lateral pressure (Figure 6), instead, it was fixed on the lateral face of the model. A concentrated force F was then applied on the rigid plate that originates a distributed load per unit area, $p = F/h^2$. Five different levels were hypothesized for F that yield the following values of p: in the case of pure compression, p = 0.05, 0.1, 0.5, 1.0, and 1.5 MPa, and in the case of shear load and lateral pressure, p = 0.01, 0.05, 0.1, 0.2, and 0.5 MPa, which are consistent with those hypothesized in previous studies[19,25−27] (Figures 4−6). According to Boccaccio et al. (2011),[51] the force F was ramped over a time period of 1 s, which is a possible time interval in which a bone tissue scaffold can be loaded. All of the three hypothesized boundary and loading conditions were also applied to the model with randomly oriented beams (control) (Figure 7e−g).

A python script was written that, given in input to Abaqus, allows all of the above-described procedures to be implemented automatically: importation of the *.sat model, modeling of the material properties, generation of the granulation tissue model, modeling of the boundary and loading conditions, meshing of scaffold, and granulation tissue models.

It is worth noting that the generation of the 3D CAD solid model, starting from the skeletonized load adapted scaffold structure, can be hypothetically carried out into Abaqus. However, it requires, line by line, the additional operations of building the cylinder, translating and orientating it in the correct location. Conversely, the "AddCylinder" CAD tool available in Rhinoceros allows these operations to be carried out automatically in a reliable way, thus simplifying the model generation procedure.

2.5. Modeling of Regular Scaffolds. To compare the performance, quantified as the percentage of the total scaffold volume occupied by neo-formed bony tissue, of irregular load adapted scaffolds with that of the regular ones, scaffolds based on a hexahedron unit cell (with rectangular and elliptic pores) and scaffolds including cylindrical rods were modeled too. In detail, in the case of scaffolds based on the hexahedron geometry, each unit cell can be obtained starting from a hexahedron/cubic volume and creating holes as a cut/protrusion of rectangular or elliptic edges along the coordinate axes (Figure 8a,g). The scaffold includes 4 × 4 × 4 unit cells, and each unit cell can be inscribed in a cube with the side of 637.6 μm. This same unit cell dimension was utilized by Byrne et al.,[19] which built a cubic scaffold model with a total volume of about 7 mm^3 and including 3 × 3 × 3 = 27 unit cells. While in the case of irregular scaffolds, the design parameter was the dimension D (Figures 2g, 4a, 5a, 6a, and 7a), in the case of regular scaffolds based on the hexahedron unit cell, according to a previous study,[18] the design parameter was represented by the two dimensions A and B (Figure 8a,g) of the semi-axes of the elliptic and the rectangular shapes. The models of the entire scaffold were obtained by replicating and mirroring, with respect to proper planes, the unit cell geometry (Figure 8b,h). The models of granulation tissue (Figure 8c,m) were obtained with the Boolean operation of subtraction, from the cubic volume $h \times h \times h$, the volume of the regular scaffold (Figure 8b,h). Regular scaffolds including cylindrical rods were also investigated (Figure 9). Such a scaffold geometry can be realized via the fused deposition modeling technique, a 3D printing process that deposits,

DOI: 10.1021/acsbiomaterials.9b01023
ACS Biomater. Sci. Eng. 2019, 5, 5392−5411

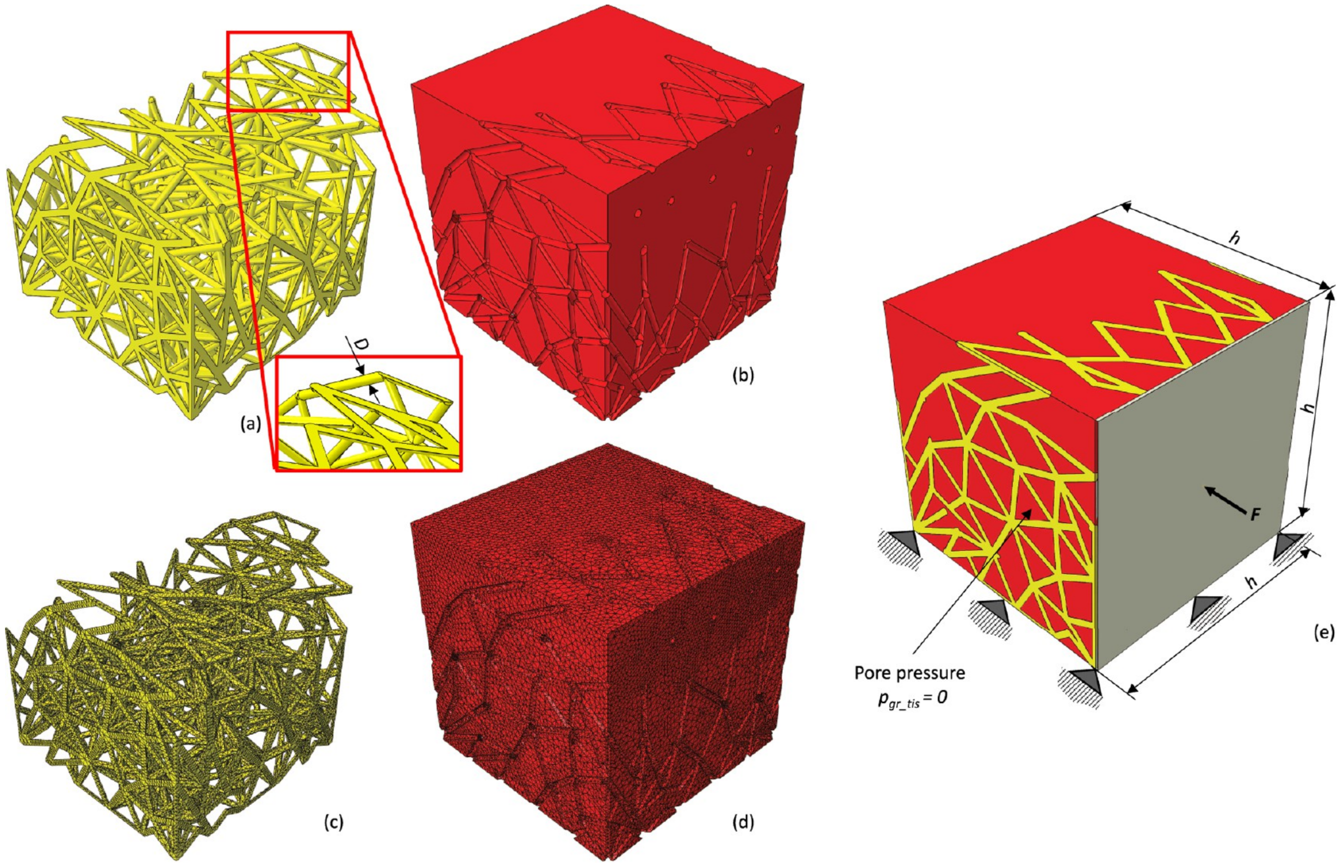

Figure 6. Models of scaffold (a) and granulation tissue (b) obtained from the structure adapted to lateral pressure were meshed with tetrahedral elements (c, d), assembled and subjected to boundary and loading conditions (e). All of the cylindrical elements had the same diameter D (a).

layer by layer, cylindrical filaments on the growing work. The filaments of each layer are perpendicular with respect to those of the adjacent one. Two different geometries of these scaffolds were built, the first including filaments with diameter $D_f = 250\ \mu$m (Figure 9a–e) and the second with filaments of diameter $D_f = 450\ \mu$m (Figure 9f–n). Scaffolds with this geometry and diameter dimensions have been tested in an in vivo study by Barba et al.[52] The design parameter that was optimized in this study was the distance $dist_{fil}$ (Figure 9a,f) between the filaments included in each layer. The modeled regular scaffolds, that possess the same dimensions $h \times h \times h$ as those of the irregular ones (Figures 8b,h and 9b,g), were subjected to the same hypothesized boundary and loading conditions of pure compression (Figures 8d,n and 9c,h), shear load (Figures 8e,o and 9d,m), and lateral pressure (Figures 8f,p and 9e,n). The same element type with the same dimensions as those utilized for the irregular structures was utilized to mesh the regular scaffolds.

Both irregular and regular scaffold models included about 5 million elements and 1 million nodes, and each finite element analysis had a duration on average of about 1.5 h on HP XW6600-Intel Xeon Dual-Processor E5-5450 3 GHz–32 Gb RAM.

2.6. Mechanobiological Model. In all of the scaffold models investigated in this study, following a previous study,[18] the granulation tissue (highlighted in red, Figures 3–9) was hypothesized to be fully and homogeneously occupied by mesenchymal stem cells. To model the biological processes taking place inside the scaffold, a mechanobiological algorithm based on deviatoric strain and fluid velocity[53] was implemented. In detail, mesenchymal stem cells were hypothesized to differentiate based on the values of a biophysical stimulus S acting on them, which assumes the following form

$$S = \frac{\gamma}{a} + \frac{\nu}{b} \tag{1}$$

where γ is the octahedral shear strain, ν is the interstitial fluid flow, and a and b are empirical constants with the values of 3.75% and 3 μm/s, respectively.[54] In detail, if ε_I, ε_{II}, and ε_{III} are the principal strains, the octahedral shear strain γ can be expressed as

$$\gamma = \frac{2}{3}\sqrt{(\varepsilon_I - \varepsilon_{II})^2 + (\varepsilon_{II} - \varepsilon_{III})^2 + (\varepsilon_I - \varepsilon_{III})^2} \tag{2}$$

Depending on the value of the stimulus S, the mesenchymal stem cells can differentiate into the following phenotypes: fibroblasts, chondrocytes, osteoblasts, or osteoclasts and hence synthesize the following tissues: fibrous tissue, cartilage, and immature and mature bone. In detail, the different tissue types are predicted to form when the following inequalities are satisfied[55]

$$\begin{cases} \text{if } S > 3 \rightarrow \text{fibroblasts (fibrous tissue)} \\ \text{elseif } 1 < S < 3 \rightarrow \text{chondrocytes (cartilage)} \\ \text{elseif } 0.53 < S < 1 \rightarrow \text{osteoblasts (immature bone)} \\ \text{elseif } 0.01 < S < 0.53 \rightarrow \text{osteoblasts (mature bone)} \\ \text{else } 0 < S < 0.01 \rightarrow \text{osteoclasts (bone resorption)} \end{cases} \tag{3}$$

2.7. Optimization Algorithm for Irregular Load Adapted Scaffolds. Two different algorithms were utilized to optimize the dimensions of the irregular load adapted scaffolds and of the regular ones. These algorithms were written in Matlab (version R2016b, Mathworks) environment and implemented to determine the optimal value of the diameter D for the irregular load adapted structures (Figure 2f), the dimensions A and B for the regular scaffolds with a hexahedron unit cell (Figure 8a,g), and the distance $dist_{fil}$ for the regular scaffolds including cylindrical filaments (Figure 9a,f). In detail, the algorithm is based on the use of the function fmincon designed to find the minimum of nonlinear multivariable functions. This function stops the research of

DOI: 10.1021/acsbiomaterials.9b01023
ACS Biomater. Sci. Eng. 2019, 5, 5392–5411

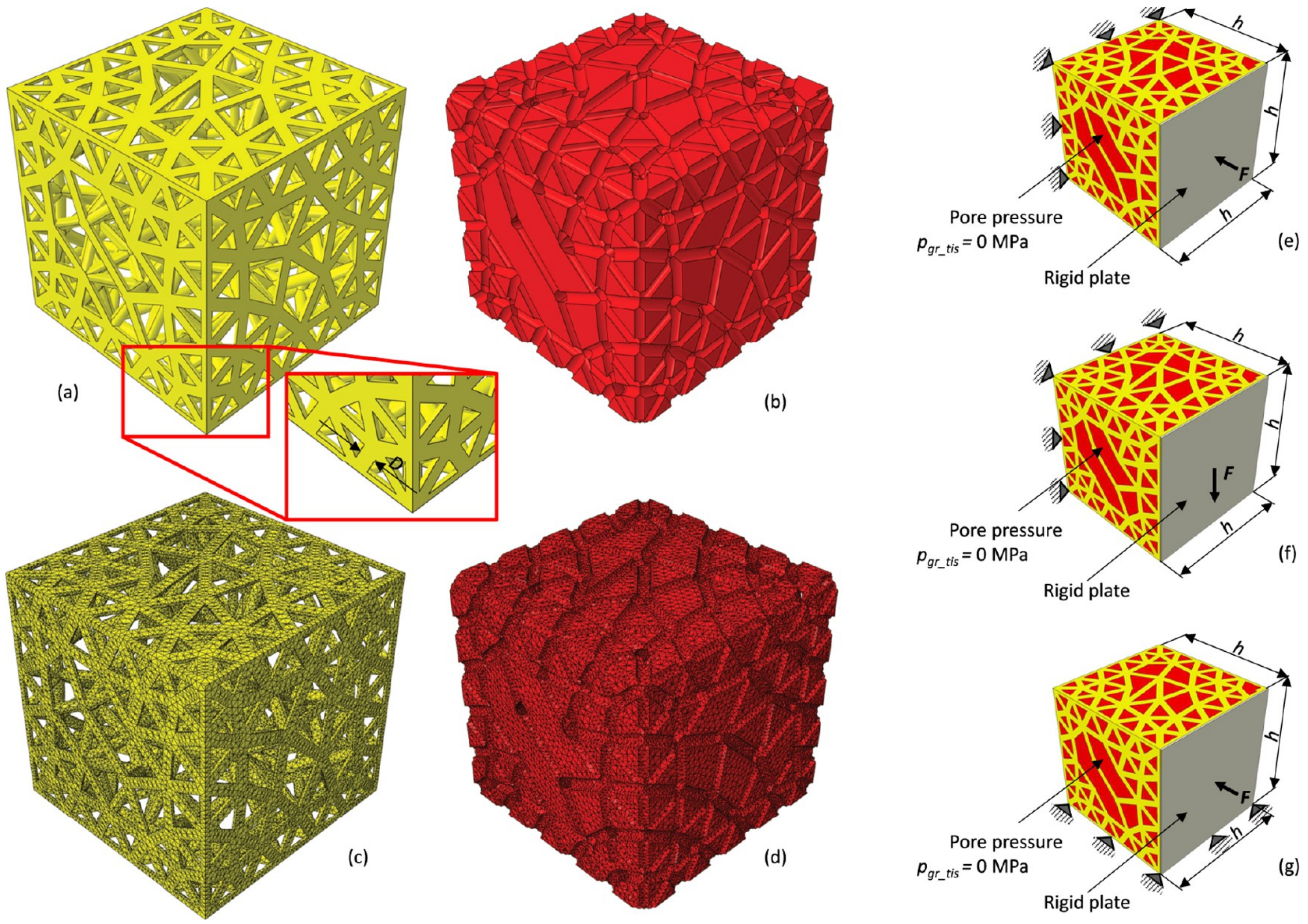

Figure 7. Models of scaffold (a) and granulation tissue (b) with beams randomly oriented (control) were meshed with tetrahedral elements (c, d), assembled and subjected to boundary and loading conditions: pure compression (e), shear (f) and lateral pressure (g). All of the cylindrical elements had the same diameter D (a).

the minimum once the stopping criteria properly defined by the user are reached.

The algorithm first requires the user to select one of the three boundary and loading conditions described above (Figure 10, block [1]). Then, the load adaptive algorithm is implemented into Ansys that builds the load adapted wireframe structure corresponding to the selected boundary and loading condition (Figure 10, block [2]). Further details on the specific macrosteps followed in Ansys are described in Figure 1 and Section 2.1. Ansys stores into a text file the coordinates of the convergence nodes and the connectivity of the line segments included in the skeletonized structure (Figure 10, block [3]). The algorithm reads the text file and copies and pastes the coordinates and the connectivity into a Python Script (PS1) (Figure 10, block [4]). A candidate solution of the diameter D is then initialized by the user (Figure 10, block [5]) and entered into the same python script PS1 (Figure 10, block [6]), which is, in turn, given in input to Rhinoceros (Figure 10, block [7]). Rhinoceros "dresses" the skeletonized structure with a 3D solid model including cylindrical elements with the diameter D equal to that initialized by the user and spherical elements with diameter $D_S = 1.1 \times D$ (Figure 10, block [8]). At the end of the execution of PS1, Rhinoceros saves the 3D model (of the sole scaffold) into .sat format (Figure 10, block [9]). Therefore, the algorithm starts the execution of a new Python Script (PS2) that is given in input to Abaqus (Figure 10, block [10]). This builds the finite element model of the scaffold and of the granulation tissue, implements the material properties (Table 1), generates the boundary and loading conditions selected above by the user, specifies the value of p, discretizes the models into finite elements, and runs the geometric nonlinear finite element analysis (Figure 10, blocks [11] and [12]). Due to the complexity of the model geometry, the virtual topology toolset available in Abaqus is used to remove all of the geometric impurities, hence favoring the subsequent process of meshing (Figure 10, block [12]). Once the finite element analysis is terminated, Abaqus, following the instructions given by PS2, stores, for each element of the granulation tissue model, the values of (i) the fluid flow velocity ν (corresponding to the magnitude of the pore fluid effective velocity vector); (ii) the principal strains ε_{I}, ε_{II}, and ε_{III}; and (iii) the element volume V_e (Figure 10, block [13]). Known these quantities and according to the eqs 1 and 2, the algorithm computes, for each element of the granulation tissue, the biophysical stimulus S and compares it with the boundaries of the mechanoregulation diagram described above (inequalities 3) (Figure 10, block [14]). For the elements where the inequality $0.01 < S < 0.53$ is satisfied, i.e., for the elements where the formation of mature bone is predicted, the algorithm stores, into a separate array Ar, the volume V_e (Figure 10, block [15]). If V_{bone} is the sum of the volumes included into Ar (Figure 10, block [16])

$$V_{bone} = \sum V_e, \quad V_e \in \mathrm{Ar} \tag{4}$$

the percentage of the scaffold volume occupied by mature bone $BO_{\%}$ can be computed as

$$BO_{\%} = \frac{V_{bone}}{V_{cube}} \times 100 = \frac{\sum V_e}{h \times h \times h} \times 100 \tag{5}$$

At this point, an optimization problem is formulated where the objective function $\Omega(D)$ is minimized (Figure 10, block [17])

$$\Omega(D) = (-1) \times BO_{\%} \tag{6}$$

DOI: 10.1021/acsbiomaterials.9b01023
ACS Biomater. Sci. Eng. 2019, 5, 5392−5411

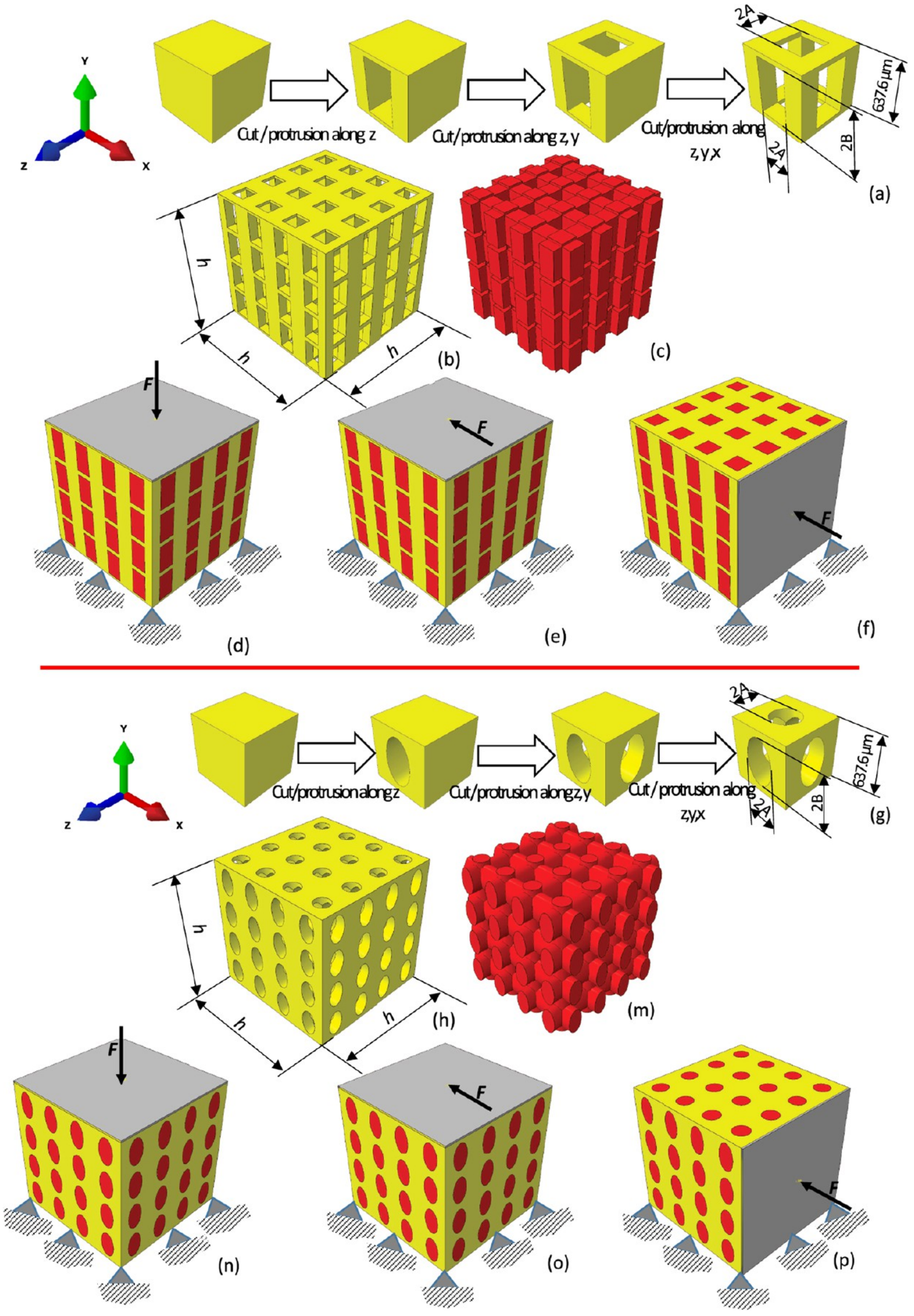

Figure 8. Each unit cell can be obtained starting from a hexahedron/cubic volume and creating holes as a cut/protrusion of rectangular (a) or elliptical (g) edges along the coordinate axes. By replicating in the space the unit cell, the models of scaffold with rectangular (b) or elliptic (h) pores were generated; the models of granulation tissue (c, m) were instead obtained with boolean operations. The scaffold models with both rectangular and elliptic pores were subjected to the same boundary and loading conditions as those hypothesized for irregular scaffolds: pure compression (d, n), shear load (e, o), and lateral pressure (f, p).

with D being the diameter of the cylindrical elements (Figures 4–7) included in the scaffolds, the design variable. In other words, in the optimization problem formulated with eq 6, the fmincon function called by the algorithm iteratively perturbs the dimension D until the lowest value of Ω (that corresponds to have the highest value of $BO_{\%}$, denoted $BO_{\%\max}$: $\min \Omega(D) = BO_{\%\max}$) is reached and hence the stopping criteria a priori established by the user are meet (Figure 10, block [18]). Once this occurs, the optimization process stops (Figure 10, block [19]) and the algorithm gives in output both the optimal value of D and the corresponding amount of bone $BO_{\%\max}$. On the contrary, if the stopping criteria are not satisfied, the algorithm iteratively perturbs the dimension of the diameter D (Figure 10, block [20]) and selects new candidate solutions (Figure 10, block [21]), thus commencing a new iteration cycle (Figure 10, block [6]). It is worth noting that eq 6 is not an explicit objective function; in other words, it does not express the design variable D in a real function. A possible strategy that can be adopted to explicit Ω in function of D is the use of surrogate models.[56,57] Very broad bounds were set to increase the design freedom of the optimization process. The lower bound $D_{\min}$ was set equal to 29 μm, while the upper one $D_{\max}$ to 200 μm.

DOI: 10.1021/acsbiomaterials.9b01023
ACS Biomater. Sci. Eng. 2019, 5, 5392–5411

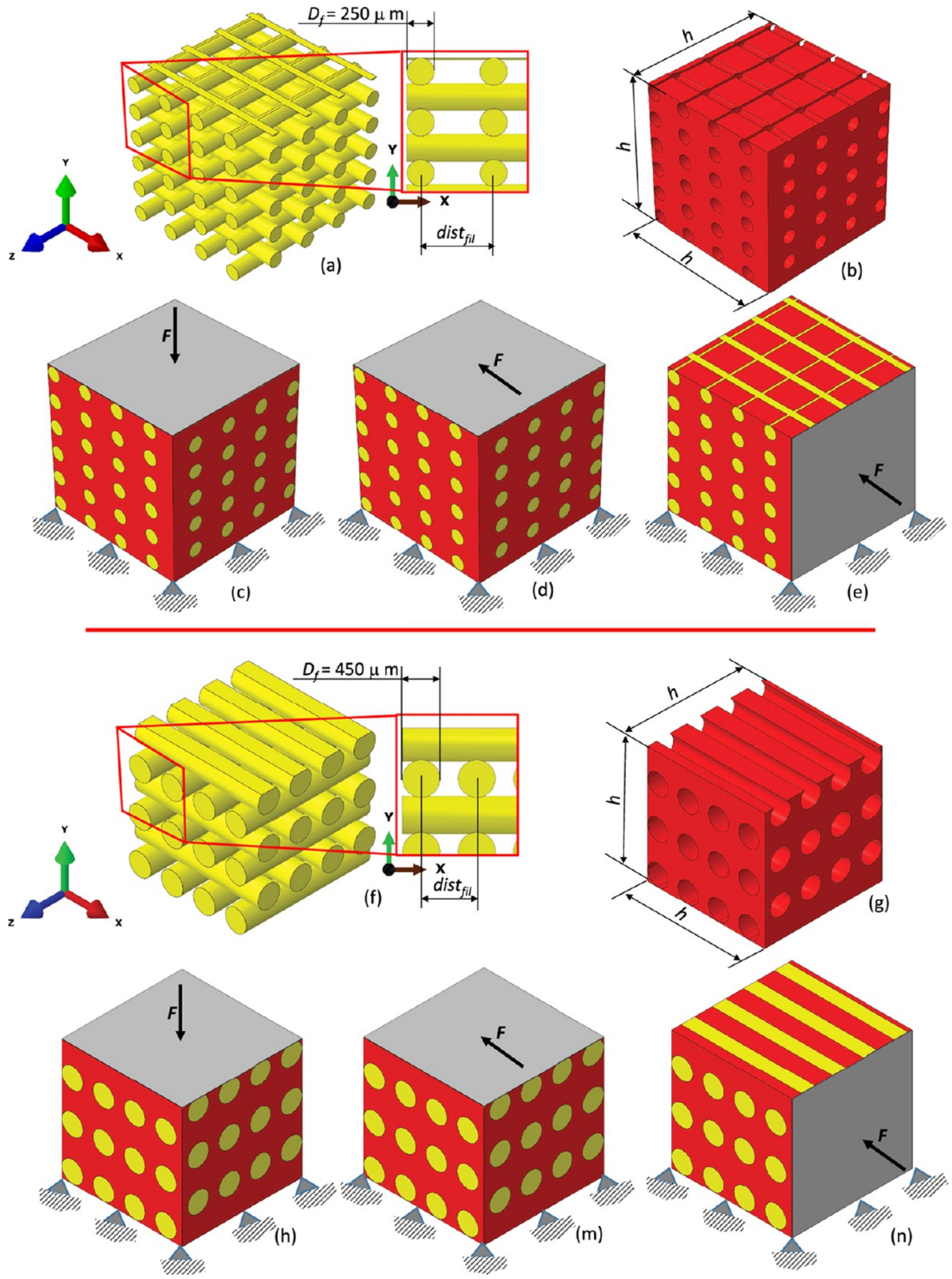

Figure 9. Scaffolds including cylindrical filaments with diameter D_f = 250 μm (a) and 450 μm (f) were built; the models of granulation tissue (b, g) were obtained with boolean operations of subtraction. The resulting scaffold models were subjected to the same boundary and loading conditions as those hypothesized for irregular scaffolds: pure compression (c, h), shear load (d, m), and lateral pressure (e, n).

fmincon has different algorithm options to determine the minimum of the objective function Ω. In this study, the sequential quadratic programing, SQP, method was chosen that uses a quasi-Newton method in which the Hessian is approximated rather than to be computed exactly. The gradient is calculated by the finite difference method that perturbs the design variable to obtain the derivatives in the objective function (Optimization Toolbox Guide, Matlab version R2016b).

2.8. Optimization Algorithm for Regular Scaffolds. The optimization algorithm utilized for the regular scaffolds differs from that implemented for the irregular ones; it does not require to build the skeletonized structure with the load adaptive algorithm as well as to dress it into Rhinoceros environment. The scaffold/granulation tissue geometry is directly built into Abaqus where geometric nonlinear finite element analyses are run. The computation of the biophysical stimulus and of the objective function $\Omega(A, B)$, for the regular scaffolds based on the hexahedron unit cell, and $\Omega(dist_{fil})$, for the regular scaffolds including cylindrical filaments, is the same as that described above (eqs 1−6). However, it is worth noting that for the irregular scaffolds, just one design variable is optimized (i.e., D) and that for the regular ones, two (i.e., A and B) in the case of scaffolds based on the hexahedron unit cell and one (i.e., $dist_{fil}$) in the case of scaffolds including cylindrical filaments.

Regular scaffolds were optimized for all of the three boundary conditions hypothesized and for all of the values of p reported above. Roughly, we can state that the optimization algorithm for regular scaffolds includes practically the only python script PS2 and the blocks [11]−[21]. However, further details on this algorithm are reported in a previous study.[18] Also, in this case, broad bounds were set to increase the design freedom of the optimization process. In detail, in the case of the scaffolds based on the hexahedron unit cell, the following values were utilized: lower bounds $A_{min} = B_{min} = 20$ μm and the upper bounds

DOI: 10.1021/acsbiomaterials.9b01023
ACS Biomater. Sci. Eng. 2019, 5, 5392−5411

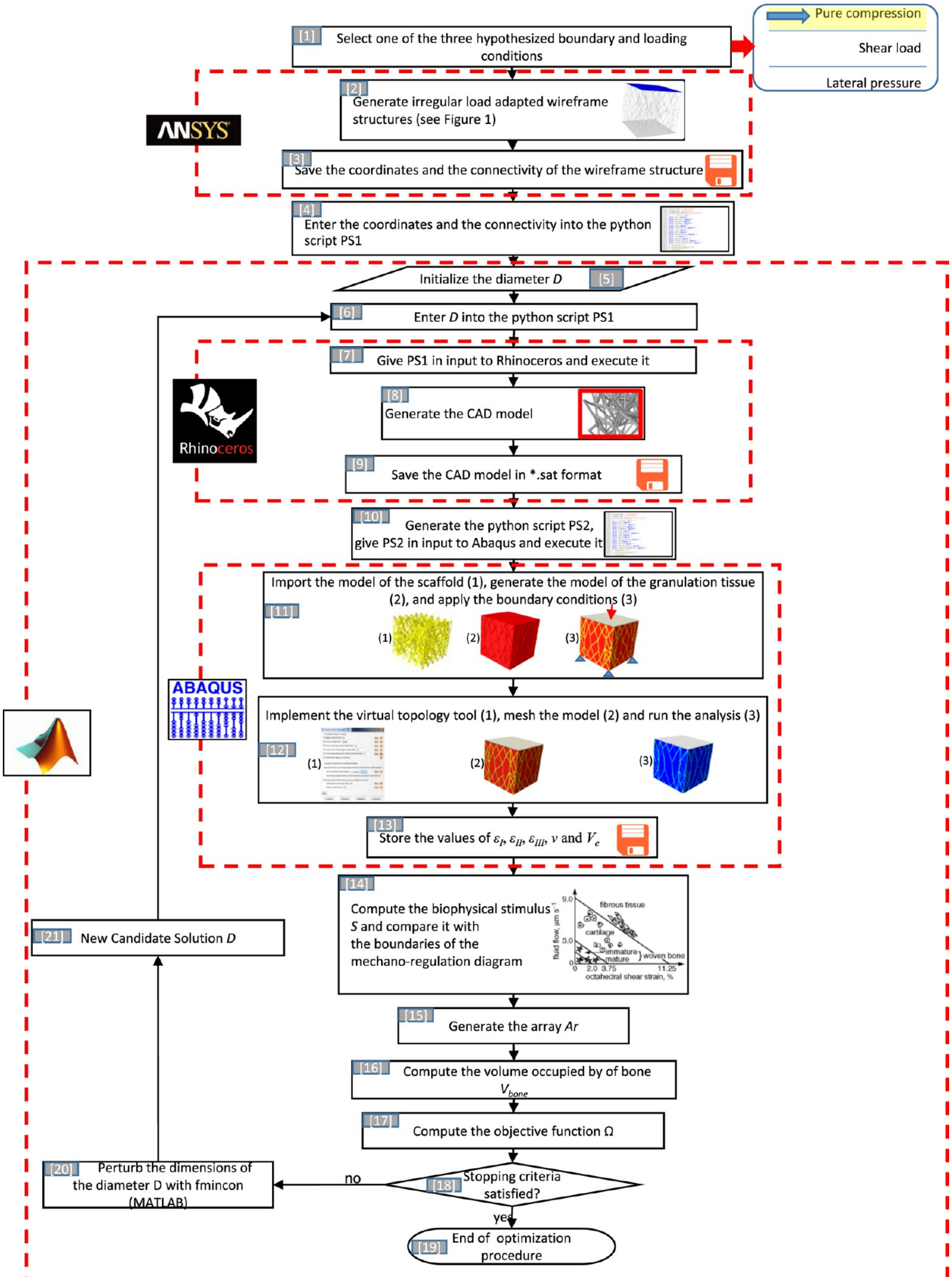

Figure 10. Schematic of the algorithm implemented to determine the optimal diameter D for the beam elements of the irregular scaffolds.

$A_{max} = B_{max} = 300$ μm. In the case of the scaffolds including cylindrical filaments: lower bound $dist_{fil\_min} = D_f$ and upper bound $dist_{fil\_max} = 1000$ μm.

The optimization algorithm for both irregular and regular scaffolds required to run, on average, at least 50 analyses to identify the correct value of D (irregular) or of A, B and $dist_{fil}$ (regular) that minimize Ω.

Considering that we hypothesized three boundary conditions and for each of them five values of p, it follows that:

- 15 optimization processes were carried out for irregular load adapted scaffolds;
- 15 for irregular randomly oriented scaffolds;
- 15 for regular scaffolds, hexahedron unit cell, rectangular pores;
- 15 for regular scaffolds, hexahedron unit cell, elliptic pores;

DOI: 10.1021/acsbiomaterials.9b01023
ACS Biomater. Sci. Eng. 2019, 5, 5392−5411

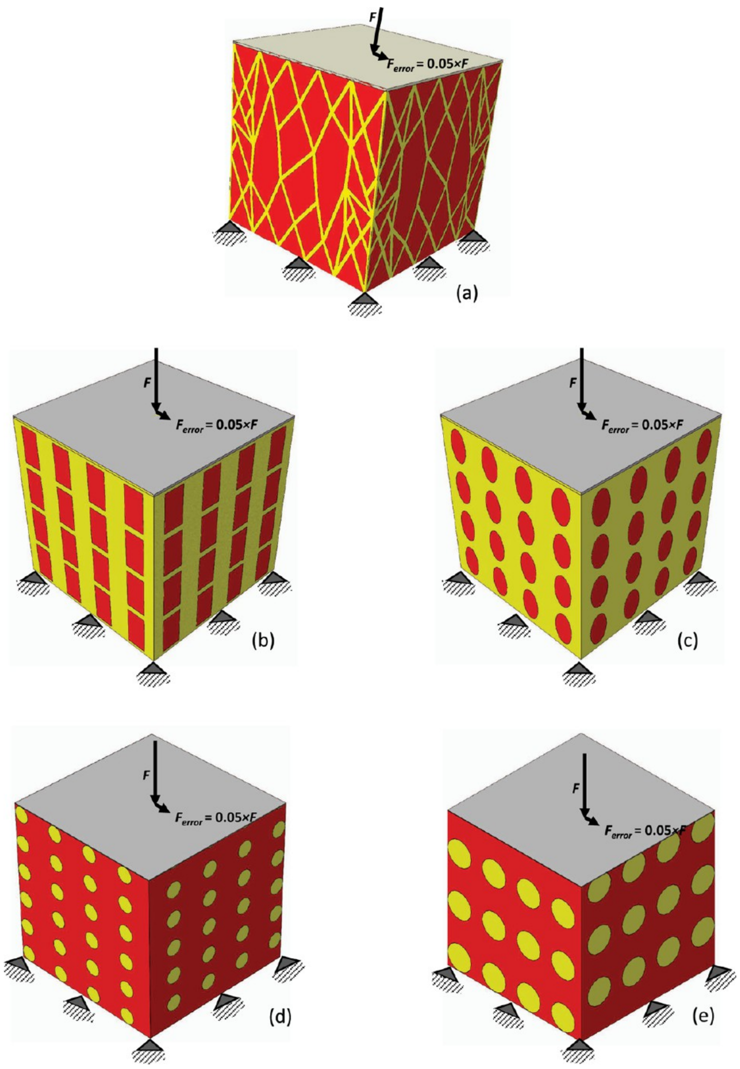

Figure 11. Boundary and loading conditions hypothesized to test the robustness of the optimized irregular load adapted (a) and regular scaffolds (b–e) including both hexahedron unit cells (b–c) and cylindrical filaments (d, e).

- 15 for regular scaffold including cylindrical filaments with D_f = 250 μm;
- 15 for regular scaffold including cylindrical filaments with D_f = 450 μm,

for a total of 90 optimization processes. Remembering that each finite element analysis lasted about 1.5 h, it follows that all of the computations carried out in this study required approximately 90 (# of optimization processes) × 50 (minimum # of analyses run in each optimization process) × 1.5 (duration in hours of each finite element analysis) = 6750 h.

2.9. Robustness of the Optimized Structures. The optimization algorithm described above allows obtaining the highest performance levels, i.e., the largest amounts of bone for specific boundary and loading conditions. However, as it is commonly known, the more a structure is optimized for specific loading conditions, the less the structure is robust with respect to unforeseen loads. Trabeculae of the spongy bone, i.e., the tissue that scaffolds replace, are oriented in the space to properly bear loads acting in specific directions. However, the increased orientation makes the spongy structures less suited to bear collateral "error" loads.[58,59] Error loads may arise because of an incorrect orientation of the scaffold in the anatomic region where it is implanted or an incorrect prediction of the boundary and loading conditions actually acting on it. We tested the robustness of the scaffolds optimized for the pure compression loading (Figure 2a), in both cases irregular (load adapted) and regular geometry. To this purpose, on the optimized scaffolds, i.e., on the models with the optimal dimension of D (irregular load adapted geometry) or with the optimal dimensions of A and B (regular geometry, hexahedron unit cell) and of $dist_{fil}$ (regular geometry, cylindrical filaments), two loads were applied: the compression load F, equal to the load for which the scaffold was optimized, and the horizontal error load equal to F_{error} = 0.05 × F (Figure 11). Such boundary conditions are consistent with those hypothesized in a previous study,[27] where horizontal and vertical loads were hypothesized to simultaneously act on the scaffold. It is worth noting that in these analyses aimed to investigate the robustness of scaffolds, no optimizations were carried out, but individual finite element analyses on previously optimized models. After each finite element analysis, the amounts of bone predicted for the specific hypothesized and optimized geometry were computed with eqs 1–5. Robustness was tested for each of the five hypothesized values of p; to this purpose, for each value of p, five individual finite element analyses were carried out, one for each of the scaffold models shown in Figure 11. Comparisons between the amounts of bone predicted $BO_{\%}$ in the presence or in the absence of the error load F_{error} were finally made.

3. RESULTS AND DISCUSSION

In this work, the performance of irregular load adapted scaffolds was investigated and compared with that of irregular randomly oriented scaffolds and regular scaffolds.

DOI: 10.1021/acsbiomaterials.9b01023
ACS Biomater. Sci. Eng. 2019, 5, 5392–5411

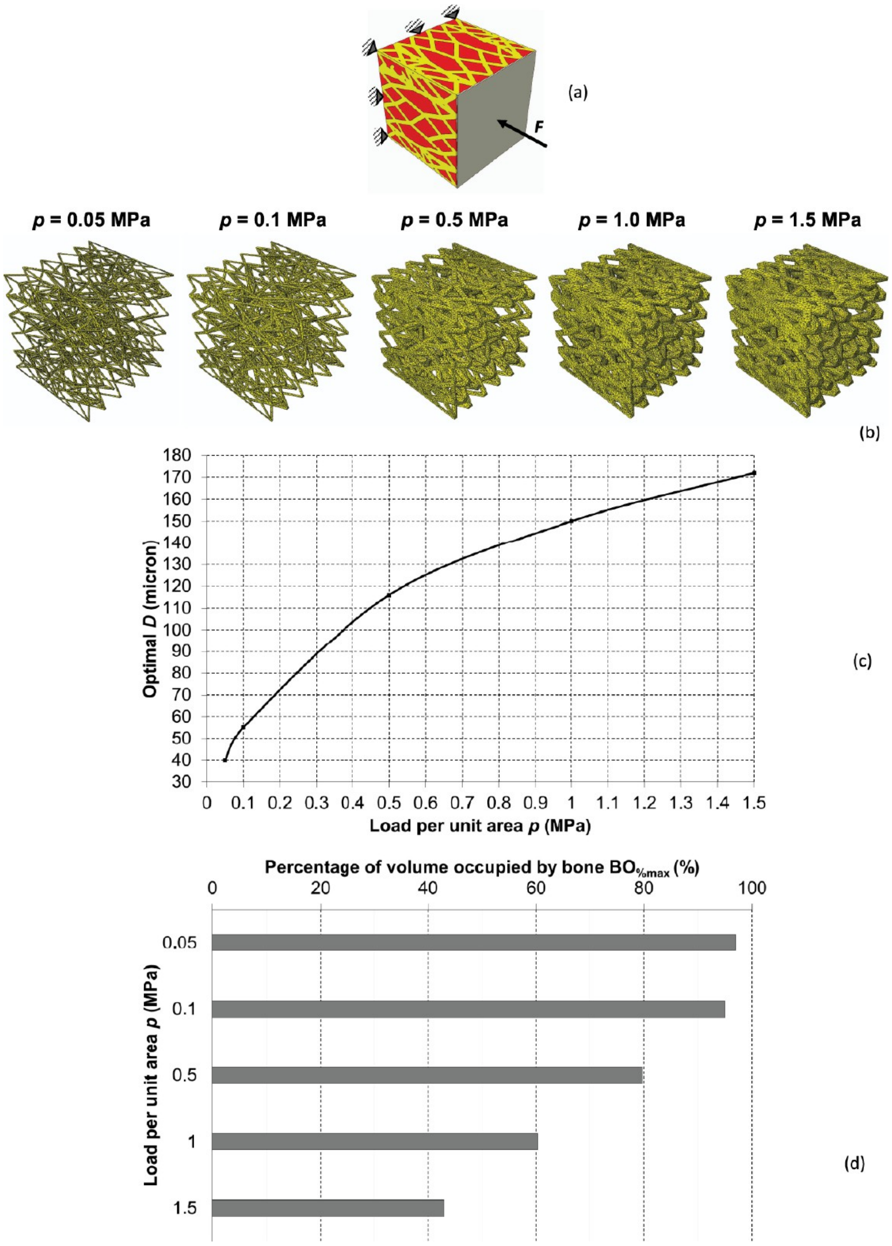

Figure 12. (b) Optimized geometries predicted by the algorithm for different levels of the load in the case of pure compression (a). Optimal diameter D (c) and $BO_{\%max}$ (d) computed for different values of p.

The patterns of the optimized structures in the case of pure compression loading are in agreement with our expectations. Scaffolds display an anisotropic distribution of beams principally oriented according to the load direction (Figure 12a). For increasing levels of load, increasing values of the optimal diameter D were predicted (Figure 12b). This result is consistent with the physics of the problem. Increasing values of p lead to increasing values of the biophysical stimulus S (eq 1) and hence to the formation of softer tissues such as fibrous and cartilaginous tissues (inequalities 3). To counterbalance this, the optimization algorithm increases the diameter D so as to minimize the strain γ, thus allowing the average stimulus to "move" toward harder tissues, i.e., the mature bone. For low load values ($p < 0.1$ MPa), large amounts of bone were predicted to create ($BO_{\%max} > 90\%$); the percentage of bone considerably decreased for medium and high load levels ($p \geq 1$ MPa).

Using the optimization algorithm for regular scaffolds outlined above, the optimal geometry of the scaffolds based on the hexahedron unit cell and of the scaffolds including cylindrical filaments was determined too. Interestingly, comparing the percentage of bone $BO_{\%max}$ computed in the case of pure compression loading for irregular and regular scaffolds, we found that the highest values were predicted just for the irregular load adapted structures (Figure 13). In detail, among the regular scaffolds, in addition to those optimized in this study, the scaffolds based on the following unit cell geometries and investigated in previous articles were considered: rhombicuboctahedron,[25] truncated cuboctahedron, truncated cube, rhombic dodecahedron, and diamond.[26] The second best scaffold immediately after the irregular load adapted one was that based on the hexahedron unit cell, rectangular pores (Figures 8b and 13).

DOI: 10.1021/acsbiomaterials.9b01023
ACS Biomater. Sci. Eng. 2019, 5, 5392−5411

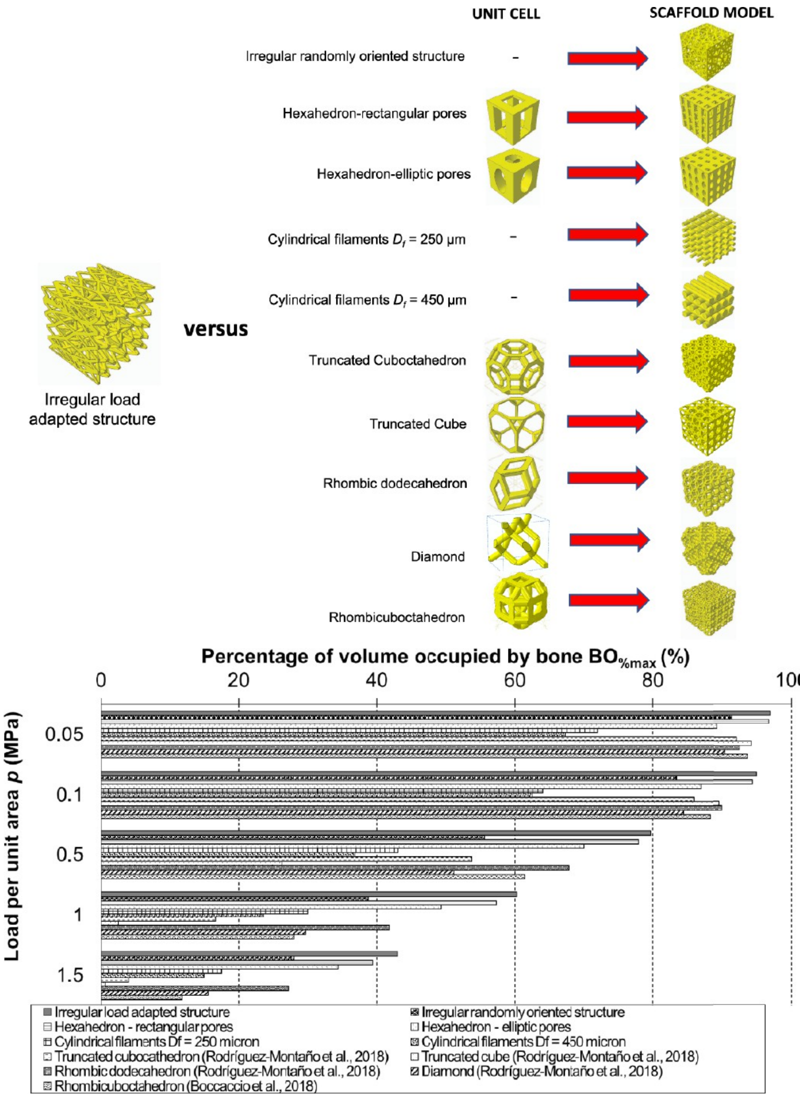

Figure 13. Comparison of $BO_{\%max}$ generated in different scaffold structures and for different levels of p in the case of pure compression loading.

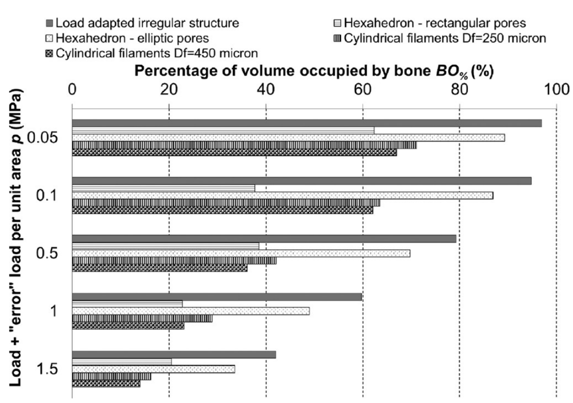

Figure 14. Comparison of $BO_{\%}$ generated in irregular and regular scaffolds in the presence of error load. It is worth noting that the error load is a horizontal load equal to 5% of the vertical compression load. For instance, for the value of $p = 0.5$ MPa, two loads act on the scaffold: a vertical force F producing a load per unit area of $p = F/(h \times h) = 0.5$ MPa and a horizontal force $F_{error} = 0.05 \times F = 0.025$ MPa.

The irregular load adapted scaffold performed better than the regular ones also in terms of robustness (Figure 14). $BO_{\%}$ predicted in the presence of error load (Figure 11) decreased marginally, with respect to the case where the error load is absent, for the irregular load adapted scaffold, for the regular scaffolds with cylindrical filaments, and for the scaffold based on the hexahedron unit cell, elliptic pores, but decreased significantly in the case of the scaffold based on the hexahedron unit cell, rectangular pores (Figure 14). This result can be justified with the argument that a structure with hexahedron unit cells, rectangular pores, behaves practically as a structure without bracings that displays, hence, an inadequate structural response to horizontal loads like the hypothesized error load F_{error}. Horizontal loads in fact, in such structures, lead to very large deformations and hence to very high values of biophysical stimulus, which implies a significant decrease of $BO_{\%}$ (Figure 14). Structures based on hexahedron unit cells, elliptic pores as well as scaffolds with filaments, instead, due to their geometric configuration, can offer an adequate structural response to the horizontal loads and are hence capable to favor the formation of large amounts of bone even in the presence of horizontal error loads. This result leads us to conclude that scaffolds based on the hexahedron unit cell, rectangular pores, can be conveniently utilized only in the cases where there is the certainty that a pure compression load acts on them. Any positioning or orientation errors done during the implantation of such regular scaffolds

DOI: 10.1021/acsbiomaterials.9b01023
ACS Biomater. Sci. Eng. 2019, 5, 5392−5411

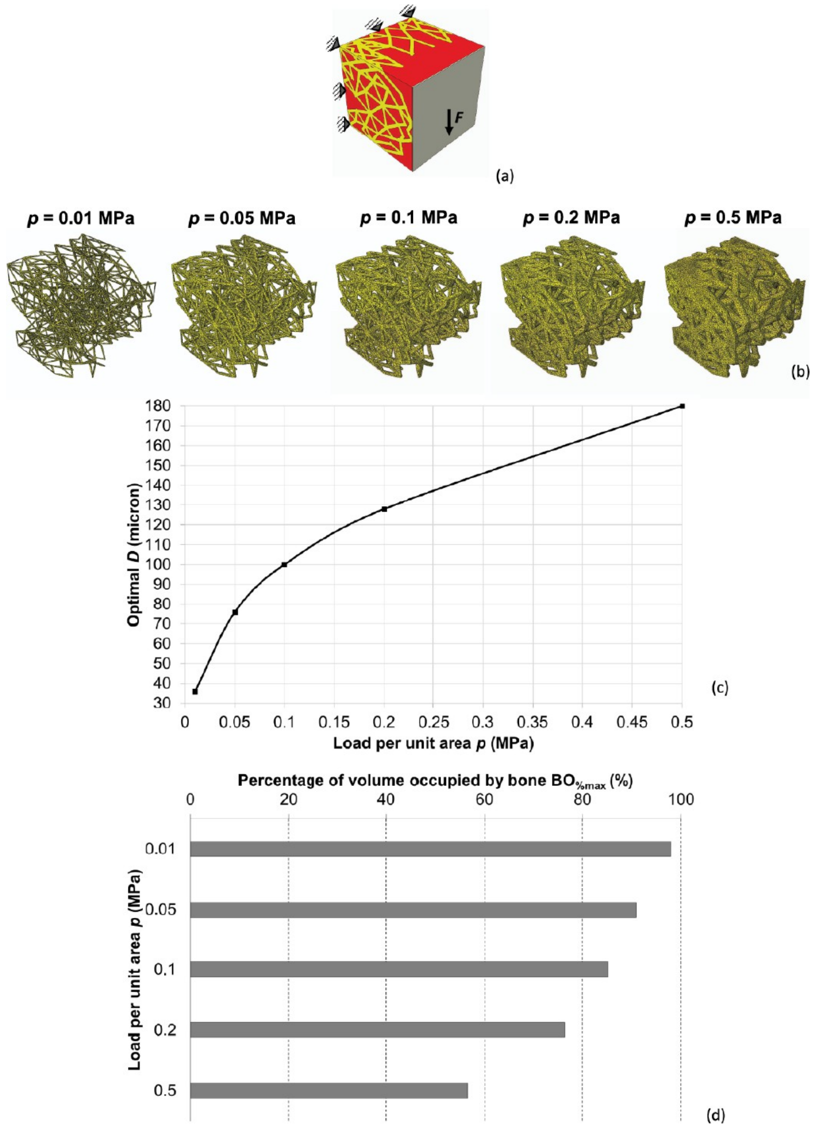

Figure 15. (b) Optimized geometries predicted by the algorithm for different levels of the load in the case of shear load (a). Values of the optimal diameter D (c) and $BO_{\%max}$ (d) for different levels of load.

would lead to an incorrect structural response and hence to the scarce formation of bone with a consequent unsuccessful regeneration process.

Also, in the case of the shear load (Figure 15) and the lateral pressure (Figure 16), increasing values of the optimal diameter D (Figures 15c and 16c, respectively) and decreasing amounts of bone $BO_{\%max}$ (Figures 15d and 16d, respectively) were predicted for increasing levels of load. This result can be justified with the argument that increasing the load, the algorithm tends to increase the dimension of the optimal diameter D, thus decreasing the volume of the pores that can be occupied by bone. The beams of the scaffold are principally distributed along the internal flux of forces induced by the hypothesized boundary conditions (Figures 15b and 16b). In particular, in the case of lateral pressure, the flux of load goes from the rigid plate where the load acts to the clamped face of the scaffold, which explains why the farthest region (from the rigid plate and from the clamped face) includes a scarce number of beams (Figure 16a).

The optimization algorithm for regular scaffolds was implemented to determine the optimal geometry of regular scaffolds (Figures 8 and 9) and subjected to shear load and lateral pressure. Comparing the amounts of bone $BO_{\%max}$, again, we found that the best scaffolds are those irregular load adapted (Figure 17a,b). However, differently from what observed in the case of pure compression, the best scaffolds, after the irregular load adapted ones, are those irregular randomly oriented that work better for medium−low loads and those regular with elliptic pores that are suited for medium−high loads. For both shear load and lateral pressure, the worst performance was that exhibited by the regular scaffolds with cylindrical filaments (Figure 17a,b). This leads us to conclude that, among the regular scaffolds, the one based on the hexahedron unit cell, rectangular pores, is more suited for bearing pure compression loads, and that the one based on the same unit cell but including elliptic pores is more suited to bear more complex load distributions. In all of the hypothesized loading conditions, the scaffolds with cylindrical filaments display poor performance, whereas the irregular load adapted ones result to be always the best.

The proposed study has some limitations. First, all of the beams of the irregular scaffolds were hypothesized to possess the same diameter D. Ideally, the optimization algorithm should optimize the dimension of the diameter of each beam included

DOI: 10.1021/acsbiomaterials.9b01023
ACS Biomater. Sci. Eng. 2019, 5, 5392−5411

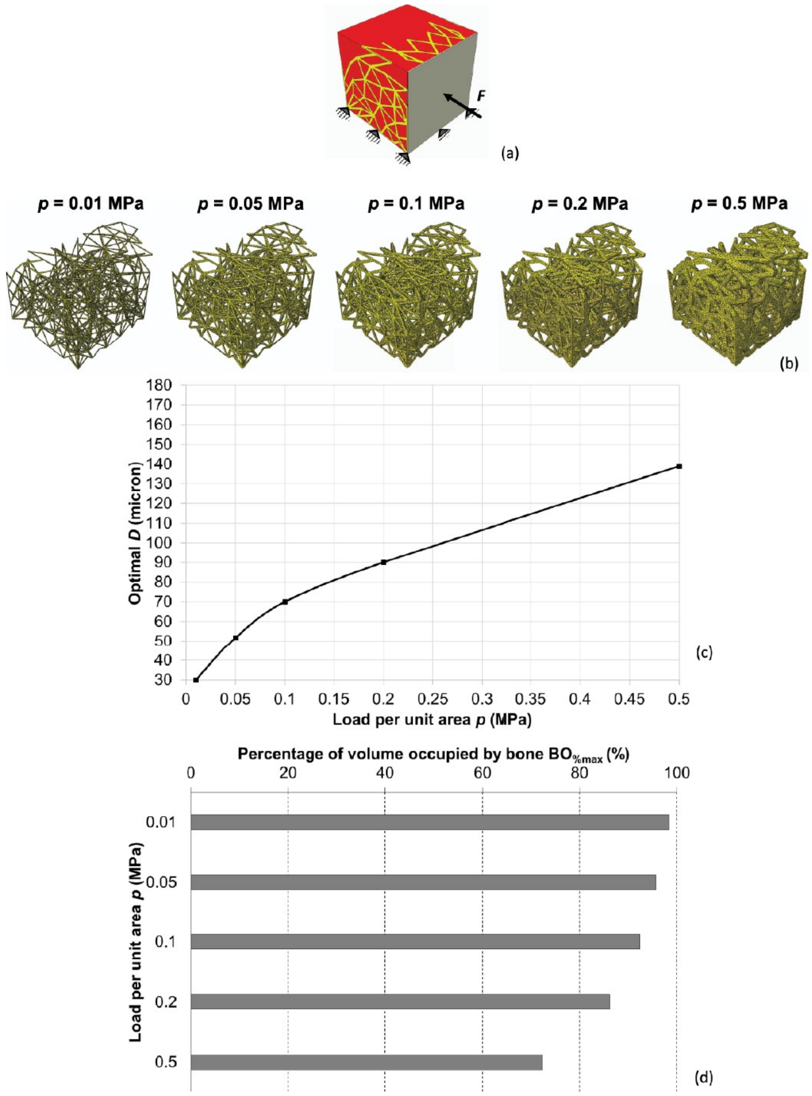

Figure 16. (b) Optimized geometries predicted by the algorithm for different levels of the load in the case of lateral pressure (a). Optimal diameter D (c) and $BO_{\%max}$ (d) computed for different values of p.

in the scaffold. However, the huge number of beams (about 1000) would lead to a large number of design variables, which implies a computational cost tremendously larger than that required in the present study. Second, the generation of the skeletonized structure by means of load adaptive algorithms follows a deterministic and not a stochastic approach. In other words, giving in input to Ansys always the same input parameters (e.g., the average number of beams (ANB), the average distance dist between the points of the cloud, the radius R_{SSS} of the spherical spaces of selection, etc.), the software always builds the same structure. This is because the algorithm implemented by Ansys to generate the cloud of points and to connect them with beams is based on the Delaunay triangulation algorithm,[60] which, in turn, is based on deterministic criteria. However, if this aspect is from one side a limitation, from the other, it can be seen as an advantage. The rationale of the triangulation algorithm of Delaunay, in fact, is to generate, in the defined convex solid (CS), the most regular geometry, that is, the most regular distribution of points and beams connecting them. Among the infinite irregular geometries that can be built with specific input parameters, the one built with the Delaunay triangulation algorithm is the most regular. In other words, the use of the Delaunay algorithm is a sort of guarantee of the regularity of the designed geometry and hence allows minimizing the geometric impurities that arise when the skeletonized structure is converted into a 3D CAD solid model. Third, no conventional techniques are currently available to fabricate the proposed irregular load adapted scaffolds, but only the rapid prototyping techniques are suited to reproduce their geometries. Future research lines should be focused on these aspects. Fourth, many bone defects are currently healed using bone substitute granules that do not provide much mechanical stability.[61] In this case, the proposed algorithm cannot be utilized to optimize such biomaterials. Fifth, the proposed optimization algorithm does not take into account the dissolution process of scaffolds. To do this, it should simulate the scaffold structural behavior in time, but this would tremendously increase the computational cost required to carry out the optimization analyses. Increases in computational power will ultimately allow simulating the scaffold dissolution process.

In spite of these limitations, the predictions of the proposed algorithm are consistent with the results of experimental studies. Liu et al.[62] found that scaffolds with an oriented microstructure implanted in rat calvarial defects stimulate the formation of

DOI: 10.1021/acsbiomaterials.9b01023
ACS Biomater. Sci. Eng. 2019, 5, 5392−5411

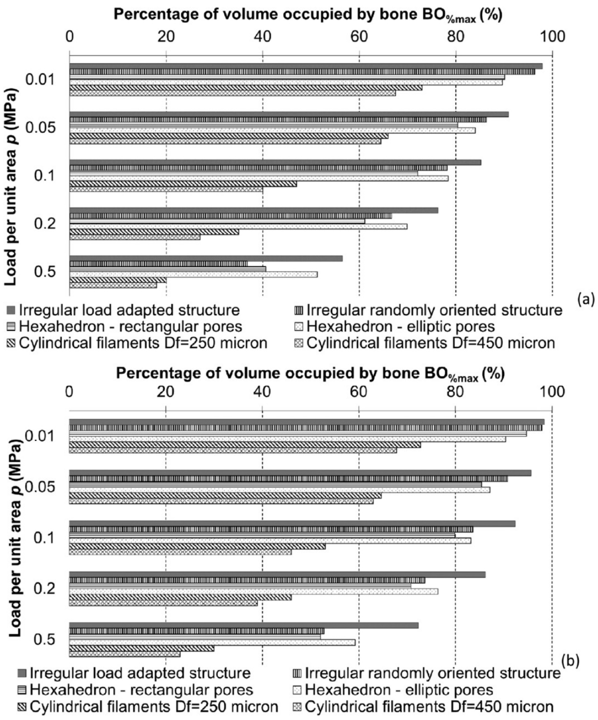

Figure 17. Comparison of $BO_{\%max}$ values predicted by the optimization algorithm for regular and irregular scaffolds in the case of (a) shear load and (b) lateral pressure.

amounts of new bone larger than those stimulated by scaffolds without a specific orientation. This is in agreement with the results obtained with the proposed computational framework. It was found, in fact, that in all of the hypothesized boundary and loading conditions the irregular load adapted scaffolds perform better than the irregular randomly oriented ones (Figures 13 and 17). In addition, the patterns of the tissues differentiating within the scaffold pores predicted by the algorithm are consistent with those observed in histological analyses. Liu et al.[62] found that in randomly oriented scaffolds, bone islands create within the scaffold pores during the regeneration process. This same behavior was observed in the randomly oriented scaffold models investigated in this study (Figure 18). Conversely, in the case of load adapted scaffolds, different patterns of tissues were predicted to form, where the bony tissue prevalently grows and develops centripetally starting from the walls of the pores toward the center (Figure 18), thus bridging the defect. Barba et al.[52] performed histological analyses on scaffolds including cylindrical filaments with diameters 250 and 450 μm and implanted in animal models. They found that the amounts of bone formed in scaffolds with diameter 250 μm are larger than those formed in scaffolds with diameter 450 μm. This is consistent with the predictions of the proposed computational framework. In all of the hypothesized boundary and loading conditions, in fact, the percentages $BO_{\%max}$ predicted for scaffolds with $D_f = 250$ μm are larger than those predicted for scaffolds with $D_f = 450$ μm (Figures 13 and 17). Furthermore, Barba et al.[52] found that randomly oriented scaffolds stimulate the formation of amounts of bone larger than those stimulated in scaffolds including cylindrical filaments. This is also consistent with our results. In fact, in all of the hypothesized boundary and loading conditions, the irregular randomly oriented scaffolds perform better than those with cylindrical filaments (Figures 13 and 17).

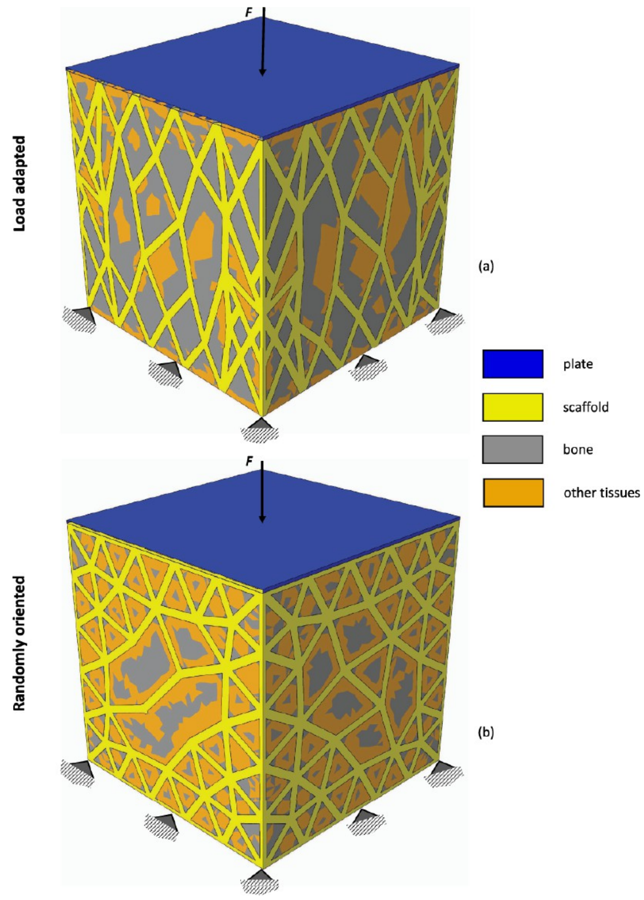

Figure 18. Patterns of tissues developing within the scaffold pores predicted by the algorithm in the case of pure compression load acting on the load adapted (a) and randomly oriented (b) scaffolds.

The proposed algorithm allows designing bioinspired scaffolds possessing mechanical properties close to those of the spongy bone. For instance, the architecture designed for irregular scaffolds adapted to the pure compression loading is characterized by having values of the ratio E_{app}/E, that is, the ratio between the apparent Young's values E_{app} (i.e., the Young's modulus of the scaffold considered in its entireness) and Young's modulus $E = 1000$ MPa (Table 1) of the material the scaffold is made from, that are consistent with those reported in the literature. To compute this ratio for different values of the diameter D, the model of the only irregular scaffold adapted to the pure compression loading (the granulation tissue was excluded) was considered. Four different values of diameter D were assigned: $D = 60, 90, 120,$ and 150 μm, which are consistent with the typical thicknesses of the trabeculae of the spongy bone[63] (Figure 19b). The structure was clamped on the bottom surface while a load (per unit area) of $p = 0.1$ MPa was imposed to the top surface through the rigid plate (Figure 19a). The resulting vertical displacement u_y (i.e., the displacement along the direction y, Figure 19a) was then determined and utilized to compute the apparent Young's modulus as $E_{app} = p/u_y \times h$ (Figure 19a). Interestingly, the computed values of the ratio E_{app}/E fall within the variability range of this ratio experimentally determined for the human spongy bone (Figure 19c). In detail, if E_{app_min} is the minimum value of E_{app} experimentally determined, E_{app_max} is the maximum value, E_{tissue} is Young's modulus of the spongy bone experimentally determined at the trabecular level, the following quantities have been considered:

DOI: 10.1021/acsbiomaterials.9b01023
ACS Biomater. Sci. Eng. 2019, 5, 5392−5411

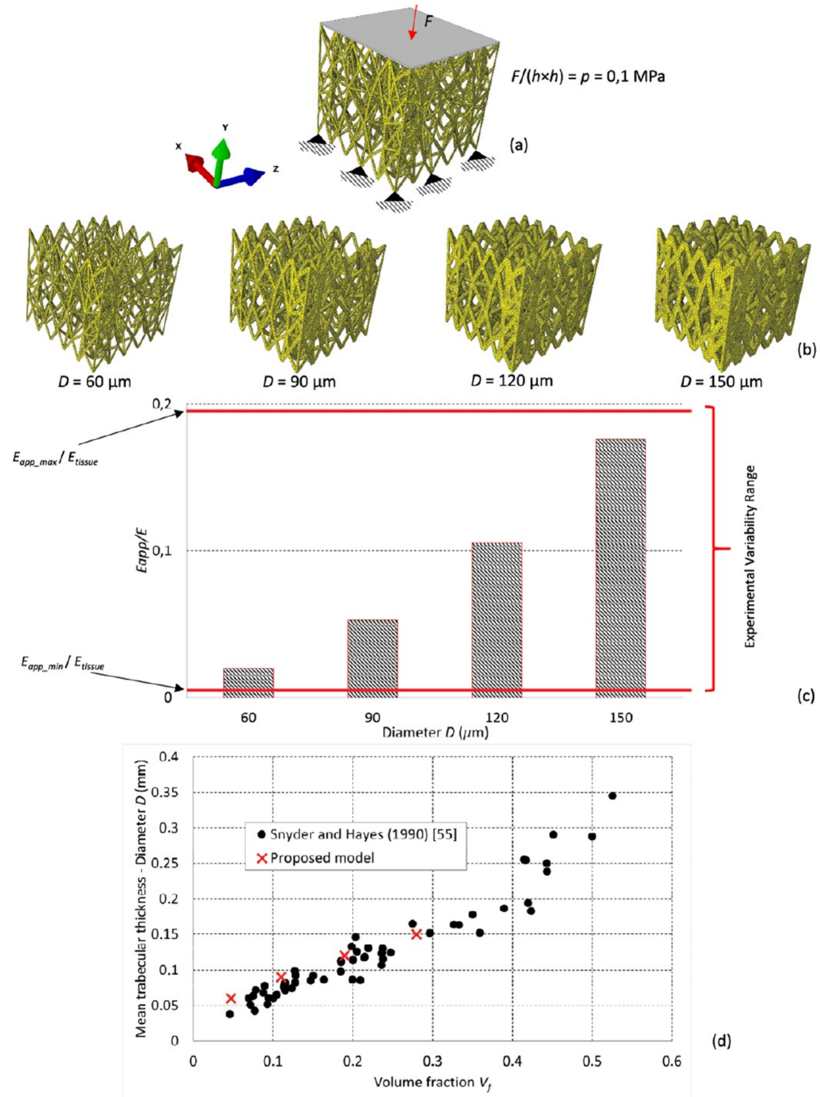

Figure 19. (a) Boundary and loading conditions utilized to determine the ratio E_{app}/E. (b) This ratio was computed for four different values of D. (c) Values of E_{app}/E computed for different D values and compared with experimental ones obtained from human spongy bone. (d) Trend of the diameter D as a function of V_f compared with that experimentally determined for the mean trabecular thickness as a function of V_f. The experimental values reported in the diagram (d) and indicated with black circles were taken from Snyder and Hayes (1990).[63] The coordinates of each point were determined with measuring tools available in Adobe Acrobat.

E_{app_min} = 60.2 MPa (which is the average value of the E_{app_min} values reported in refs 64−66);

E_{app_max} = 2725.96 MPa (which is the average value of the E_{app_max} values reported in refs 64−66);

E_{tissue} = 13.96 GPa (which is the average of the E_{tissue} values reported in refs 67−69)

which yield the following ratios: E_{app_min}/E_{tissue} = 0.0043, E_{app_max}/E_{tissue} = 0.1952 (Figure 19c). Furthermore, for each of the four scaffold models described above, the volume V_{scaff} was measured via Abaqus and divided by the total volume of the model $V_{cube} = h \times h \times h$ to determine the volume fraction $V_f = V_{scaff}/V_{cube}$. Interestingly, the trend of the diameter D expressed as a function of V_f is consistent with that experimentally determined for the mean trabecular thickness as a function of V_f (Figure 19d).[63]

In general, we found that the irregular load adapted scaffolds perform better than the irregular randomly oriented and the regular ones in all of the hypothesized boundary and loading conditions. Irregular load adapted scaffolds were predicted also to be the most robust structures, which means that they can favor the formation of large amounts of bone even in the case when they are subjected to boundary and loading conditions slightly different with respect to those utilized for their optimization (Figure 12).

4. CONCLUSIONS

Load adaptive and mechanobiological algorithms were combined to design and optimize irregular load adapted scaffolds for bone tissue engineering. The performance of these scaffolds, quantified in terms of amounts of neo-formed bone, was compared with that of irregular randomly oriented scaffolds and regular scaffolds. Different boundary and loading conditions were hypothesized to act on the scaffolds, and in all of them, the irregular load adapted scaffolds were predicted to perform better than the others. Interestingly, the predictions of the proposed optimization algorithm are consistent with the histological observations and the results of experimental studies. The proposed computational framework appears to be a valid

DOI: 10.1021/acsbiomaterials.9b01023
ACS Biomater. Sci. Eng. 2019, 5, 5392−5411

tool that can be utilized to design and optimize high-performance scaffolds suited to bear even complex load distributions.

AUTHOR INFORMATION

Corresponding Author

*E-mail: antonio.boccaccio@poliba.it.

ORCID

Francesco Naddeo: 0000-0003-0017-6631
Antonio Boccaccio: 0000-0002-9623-7189

Notes

The authors declare no competing financial interest.

ACKNOWLEDGMENTS

This research has been made possible by the collaboration between Universidad Nacional de Colombia, Polytechnic University of Bari, and University of Salerno and was supported by a Ph.D. grant from Colombian Institute for Science and Research COLCIENCIAS (Grant 647-2015).

REFERENCES

(1) Moreno, M.; Amaral, M. H.; M Sousa Lobo, J.; C Silva, A. Scaffolds for bone regeneration: state of the art. *Curr. Pharm. Des.* **2016**, *22*, 2726−2736.
(2) Roseti, L.; Parisi, V.; Petretta, M.; Cavallo, C.; Desando, G.; Bartolotti, I.; Grigolo, B. Scaffolds for Bone Tissue Engineering: State of the art and new perspectives. *Mater. Sci. Eng., C* **2017**, *78*, 1246−1262.
(3) Boccaccio, A.; Ballini, A.; Pappalettere, C.; Tullo, D.; Cantore, S.; Desiate, A. Finite element method (FEM), mechanobiology and biomimetic scaffolds in bone tissue engineering. *Int. J. Biol. Sci.* **2011**, *7*, 112−132.
(4) Giannitelli, S.; Accoto, D.; Trombetta, M.; Rainer, A. Current trends in the design of scaffolds for computer-aided tissue engineering. *Acta Biomater.* **2014**, *10*, 580−594.
(5) Gariboldi, M. I.; Best, S. M. Effect of ceramic scaffold architectural parameters on biological response. *Front. Bioeng. Biotechnol.* **2015**, *3*, 151.
(6) Chatzidai, N.; Karalekas, D. A Computational Based Design and Optimization Study of Scaffold Architectures. In *Applications of Computational Tools in Biosciences and Medical Engineering*; Springer, 2015; pp 1−17.
(7) Perez, R. A.; Mestres, G. Role of pore size and morphology in musculo-skeletal tissue regeneration. *Mater. Sci. Eng., C* **2016**, *61*, 922−939.
(8) Turnbull, G.; Clarke, J.; Picard, F.; Riches, P.; Jia, L.; Han, F.; Li, B.; Shu, W. 3D bioactive composite scaffolds for bone tissue engineering. *Bioact. Mater.* **2017**, DOI: 10.1016/j.bioactmat.2017.10.001.
(9) Wu, T.; Yu, S.; Chen, D.; Wang, Y. Bionic design, materials and performance of bone tissue scaffolds. *Materials* **2017**, *10*, 1187.
(10) Dias, M. R.; Guedes, J. M.; Flanagan, C. L.; Hollister, S. J.; Fernandes, P. R. Optimization of scaffold design for bone tissue engineering: a computational and experimental study. *Med. Eng. Phys.* **2014**, *36*, 448−457.
(11) Coelho, P. G.; Hollister, S. J.; Flanagan, C. L.; Fernandes, P. R. Bioresorbable scaffolds for bone tissue engineering: optimal design, fabrication, mechanical testing and scale-size effects analysis. *Med. Eng. Phys.* **2015**, *37*, 287−296.
(12) Lacroix, D.; Planell, J. A.; Prendergast, P. J. Computer-aided design and finite-element modelling of biomaterial scaffolds for bone tissue engineering. *Philos. Trans. R. Soc., A* **2009**, *367*, 1993−2009.
(13) Adachi, T.; Osako, Y.; Tanaka, M.; Hojo, M.; Hollister, S. J. Framework for optimal design of porous scaffold microstructure by computational simulation of bone regeneration. *Biomaterials* **2006**, *27*, 3964−3972.
(14) Sandino, C.; Planell, J.; Lacroix, D. A finite element study of mechanical stimuli in scaffolds for bone tissue engineering. *J. Biomech.* **2008**, *41*, 1005−1014.
(15) Olivares, A. L.; Marsal, È.; Planell, J. A.; Lacroix, D. Finite element study of scaffold architecture design and culture conditions for tissue engineering. *Biomaterials* **2009**, *30*, 6142−6149.
(16) Milan, J.-L.; Planell, J. A.; Lacroix, D. Simulation of bone tissue formation within a porous scaffold under dynamic compression. *Biomech. Model. Mechanobiol.* **2010**, *9*, 583−596.
(17) Chen, Y.; Zhou, S.; Li, Q. Microstructure design of biodegradable scaffold and its effect on tissue regeneration. *Biomaterials* **2011**, *32*, 5003−5014.
(18) Boccaccio, A.; Uva, A. E.; Fiorentino, M.; Lamberti, L.; Monno, G. A mechanobiology-based algorithm to optimize the microstructure geometry of bone tissue scaffolds. *Int. J. Biol. Sci.* **2016**, *12*, 1−17.
(19) Byrne, D. P.; Lacroix, D.; Planell, J. A.; Kelly, D. J.; Prendergast, P. J. Simulation of tissue differentiation in a scaffold as a function of porosity, Young's modulus and dissolution rate: application of mechanobiological models in tissue engineering. *Biomaterials* **2007**, *28*, 5544−5554.
(20) Medine, C. N.; Khan, F.; Pernagallo, S.; Zhang, R.; Tura, O.; Bradley, M.; Hay, D. C. Identification and Application of Polymers as Biomaterials for Tissue Engineering and Regenerative Medicine. In *Biomaterials and Stem Cells in Regenerative Medicine*; CRC Press, 2012; Vo. *1*.
(21) Ahmadi, S. M.; Yavari, S. A.; Wauthle, R.; Pouran, B.; Schrooten, J.; Weinans, H.; Zadpoor, A. A. Additively manufactured open-cell porous biomaterials made from six different space-filling unit cells: The mechanical and morphological properties. *Materials* **2015**, *8*, 1871−1896.
(22) Yu, G. Z.; Chou, D.-T.; Hong, D.; Roy, A.; Kumta, P. N. Biomimetic rotated lamellar plywood motifs by additive manufacturing of metal alloy scaffolds for bone tissue engineering. *ACS Biomater. Sci. Eng.* **2017**, *3*, 648−657.
(23) Zhai, X.; Ma, Y.; Hou, C.; Gao, F.; Zhang, Y.; Ruan, C.; Pan, H.; Lu, W. W.; Liu, W. 3D-printed high strength bioactive supramolecular polymer/clay nanocomposite hydrogel scaffold for bone regeneration. *ACS Biomater. Sci. Eng.* **2017**, *3*, 1109−1118.
(24) Zadpoor, A. A.; Hedayati, R. Analytical relationships for prediction of the mechanical properties of additively manufactured porous biomaterials. *J. Biomed. Mater. Res., Part A* **2016**, *104*, 3164−3174.
(25) Boccaccio, A.; Fiorentino, M.; Uva, A. E.; Laghetti, L. N.; Monno, G. Rhombicuboctahedron unit cell based scaffolds for bone regeneration: geometry optimization with a mechanobiology − driven algorithm. *Mater. Sci. Eng., C* **2018**, *83*, 51−66.
(26) Rodríguez-Montaño, Ó. L.; Cortés-Rodríguez, C. J.; Uva, A. E.; Fiorentino, M.; Gattullo, M.; Monno, G.; Boccaccio, A. Comparison of the mechanobiological performance of bone tissue scaffolds based on different unit cell geometries. *J. Mech. Behav. Biomed. Mater.* **2018**, *83*, 28−45.
(27) Boccaccio, A.; Uva, A. E.; Fiorentino, M.; Mori, G.; Monno, G. Geometry design optimization of functionally graded scaffolds for bone tissue engineering: A mechanobiological approach. *PLoS One* **2016**, *11*, No. e0146935.
(28) Naddeo, F.; Cappetti, N.; Naddeo, A. Novel "load adaptive algorithm based" procedure for 3D printing of cancellous bone-inspired structures. *Composites, Part B* **2017**, *115*, 60−69.
(29) Naddeo, F.; Naddeo, A.; Cappetti, N. Novel "load adaptive algorithm based" procedure for 3D printing of lattice-based components showing parametric curved micro-beams. *Composites, Part B* **2017**, *115*, 51−59.
(30) Rainer, A.; Giannitelli, S. M.; Accoto, D.; De Porcellinis, S.; Guglielmelli, E.; Trombetta, M. Load-adaptive scaffold architecturing: a bioinspired approach to the design of porous additively manufactured scaffolds with optimized mechanical properties. *Ann. Biomed. Eng.* **2012**, *40*, 966−975.
(31) Guan, J.; Fujimoto, K. L.; Sacks, M. S.; Wagner, W. R. Preparation and characterization of highly porous, biodegradable

polyurethane scaffolds for soft tissue applications. *Biomaterials* **2005**, *26*, 3961−3971.
(32) Doustgani, A.; Vasheghani-Farahani, E.; Soleimani, M. Aligned and random nanofibrous nanocomposite scaffolds for bone tissue engineering. *Nanomed. J.* **2013**, *1*, 20−27.
(33) Scaglione, S.; Giannoni, P.; Bianchini, P.; Sandri, M.; Marotta, R.; Firpo, G.; Valbusa, U.; Tampieri, A.; Diaspro, A.; Bianco, P.; et al. Order versus Disorder: in vivo bone formation within osteoconductive scaffolds. *Sci. Rep.* **2012**, *2*, No. 274.
(34) Wang, X.; Ding, B.; Li, B. Biomimetic electrospun nanofibrous structures for tissue engineering. *Mater. today* **2013**, *16*, 229−241.
(35) Sarker, B.; Li, W.; Zheng, K.; Detsch, R.; Boccaccini, A. R. Designing porous bone tissue engineering scaffolds with enhanced mechanical properties from composite hydrogels composed of modified alginate, gelatin, and bioactive glass. *ACS Biomater. Sci. Eng.* **2016**, *2*, 2240−2254.
(36) Goyal, R.; Guvendiren, M.; Freeman, O.; Mao, Y.; Kohn, J. Optimization of polymer-ecm composite scaffolds for tissue engineering: effect of cells and culture conditions on polymeric nanofiber mats. *J. Funct. Biomater.* **2017**, *8*, 1.
(37) Novajra, G.; Perdika, P.; Pisano, R.; Miola, M.; Bari, A.; Jones, J.; Detsch, R.; Boccaccini, A.; Vitale-Brovarone, C. Structure optimisation and biological evaluation of bone scaffolds prepared by co-sintering of silicate and phosphate glasses. *Adv. Appl. Ceram.* **2015**, *114*, S48−S55.
(38) Anindyajati, A.; Boughton, P.; Ruys, A. J. Modelling and optimization of Polycaprolactone ultrafine-fibres electrospinning process using response surface methodology. *Materials* **2018**, *11*, 441.
(39) Scaffaro, R.; Sutera, F.; Lopresti, F. Using Taguchi method for the optimization of processing variables to prepare porous scaffolds by combined melt mixing/particulate leaching. *Mater. Des.* **2017**, *131*, 334−342.
(40) Gupta, P.; Nayak, K. K. Optimization of keratin/alginate scaffold using RSM and its characterization for tissue engineering. *Int. J. Biol. Macromol.* **2016**, *85*, 141−149.
(41) Tanaka, Y.; Yamaoka, H.; Nishizawa, S.; Nagata, S.; Ogasawara, T.; Asawa, Y.; Fujihara, Y.; Takato, T.; Hoshi, K. The optimization of porous polymeric scaffolds for chondrocyte/atelocollagen based tissue-engineered cartilage. *Biomaterials* **2010**, *31*, 4506−4516.
(42) Tajsoleiman, T.; Abdekhodaie, M. J.; Gernaey, K. V.; Krühne, U. Geometry optimization of a fibrous scaffold based on mathematical modelling and CFD simulation of a dynamic cell culture. In *Computer Aided Chemical Engineering*; Elsevier, 2016; Vol. *38*, pp 1413−1418.
(43) Almeida, H. A.; Bártolo, P. J. Combined Elastic and Shear Stress Solicitations for Topological Optimisation of Micro-CT Based Scaffolds. *Procedia Eng.* **2015**, *110*, 159−166.
(44) Patton, K. T. *Anatomy Physiology-E-Book*; Elsevier Health Sciences: 2015.
(45) Wolff, J. *The Law of Bone Remodelling*; Springer: New York, 1986; Vol. *1*, p 8; Translated by P. Maquet; R. Furlong.
(46) Zhang, C.; Mcadams, D. A.; Grunlan, J. C. Nano/Micro-Manufacturing of Bioinspired Materials: a Review of Methods to Mimic Natural Structures. *Adv. Mater.* **2016**, *28*, 6292−6321.
(47) Cricrì, G.; Garofalo, E.; Naddeo, F.; Incarnato, L. Stiffness constants prediction of nanocomposites using a periodic 3D-FEM model. *J. Polym. Sci., Part B: Polym. Phys.* **2012**, *50*, 207−220.
(48) Lakatos, É.; Bojtár, I. Trabecular bone adaptation in a finite element frame model using load dependent fabric tensors. *Mech. Mater.* **2012**, *44*, 130−138.
(49) Pothuaud, L.; Porion, P.; Lespessailles, E.; Benhamou, C.; Levitz, P. A new method for three-dimensional skeleton graph analysis of porous media: application to trabecular bone microarchitecture. *J. Microsc.* **2000**, *199*, 149−161.
(50) Stauber, M.; Müller, R. Age-related changes in trabecular bone microstructures: global and local morphometry. *Osteoporosis Int.* **2006**, *17*, 616−626.
(51) Boccaccio, A.; Kelly, D. J.; Pappalettere, C. A mechano-regulation model of fracture repair in vertebral bodies. *J. Orthop. Res.* **2011**, *29*, 433−443.
(52) Barba, A.; Maazouz, Y.; Diez-Escudero, A.; Rappe, K.; Espanol, M.; Montufar, E. B.; Öhman-Mägi, C.; Persson, C.; Fontecha, P.; Manzanares, M.-C.; et al. Osteogenesis by foamed and 3D-printed nanostructured calcium phosphate scaffolds: Effect of pore architecture. *Acta Biomater.* **2018**, *79*, 135−147.
(53) Prendergast, P.; Huiskes, R.; Søballe, K. Biophysical stimuli on cells during tissue differentiation at implant interfaces. *J. Biomech.* **1997**, *30*, 539−548.
(54) Huiskes, R.; Van Driel, W.; Prendergast, P.; Søballe, K. A biomechanical regulatory model for periprosthetic fibrous-tissue differentiation. *J. Mater. Sci.: Mater. Med.* **1997**, *8*, 785−788.
(55) Lacroix, D.; Prendergast, P. A mechano-regulation model for tissue differentiation during fracture healing: analysis of gap size and loading. *J. Biomech.* **2002**, *35*, 1163−1171.
(56) Rungsiyakull, C.; Li, Q.; Sun, G.; Li, W.; Swain, M. V. Surface morphology optimization for osseointegration of coated implants. *Biomaterials* **2010**, *31*, 7196−7204.
(57) Chen, J.; Rungsiyakull, C.; Li, W.; Chen, Y.; Swain, M.; Li, Q. Multiscale design of surface morphological gradient for osseointegration. *J. Mech. Behav. Biomed. Mater.* **2013**, *20*, 387−397.
(58) Homminga, J.; Van-Rietbergen, B.; Lochmüller, E.-M.; Weinans, H.; Eckstein, F.; Huiskes, R. The osteoporotic vertebral structure is well adapted to the loads of daily life, but not to infrequent "error" loads. *Bone* **2004**, *34*, 510−516.
(59) Bucher, C. Robustness analysis in structural optimization. *Struct. Infrastruct. Eng.* **2009**, *5*, 287−293.
(60) *Ansys. 16.2 Documentation for ANSYS*. Theory reference, 2015.
(61) Rolvien, T.; Barbeck, M.; Wenisch, S.; Amling, M.; Krause, M. Cellular mechanisms responsible for success and failure of bone substitute materials. *Int. J. Mol. Sci.* **2018**, *19*, 2893.
(62) Liu, X.; Rahaman, M. N.; Fu, Q. Bone regeneration in strong porous bioactive glass (13-93) scaffolds with an oriented microstructure implanted in rat calvarial defects. *Acta Biomater.* **2013**, *9*, 4889−4898.
(63) Snyder, B. D.; Hayes, W. C. Multiaxial structure-property relations in trabecular bone. *Biomech. Diarthrodial Jt.* **1990**, 31−59.
(64) Ducheyne, P.; Heymans, L.; Martens, M.; Aernoudt, E.; de Meester, P.; Mulier, J. C. The mechanical behaviour of intracondylar cancellous bone of the femur at different loading rates. *J. Biomech.* **1977**, *10*, 747−762.
(65) Martens, M.; Van Audekercke, R.; Delport, P.; De Meester, P.; Mulier, J. The mechanical characteristics of cancellous bone at the upper femoral region. *J. Biomech.* **1983**, *16*, 971−983.
(66) Chevalier, Y.; Pahr, D.; Allmer, H.; Charlebois, M.; Zysset, P. Validation of a voxel-based FE method for prediction of the uniaxial apparent modulus of human trabecular bone using macroscopic mechanical tests and nanoindentation. *J. Biomech.* **2007**, *40*, 3333−3340.
(67) Ashman, R. B.; Rho, J. Y. Elastic modulus of trabecular bone material. *J. Biomech.* **1988**, *21*, 177−181.
(68) Turner, C. H.; Rho, J.; Takano, Y.; Tsui, T. Y.; Pharr, G. M. The elastic properties of trabecular and cortical bone tissues are similar: results from two microscopic measurement techniques. *J. Biomech.* **1999**, *32*, 437−441.
(69) Zysset, P. K.; Guo, X. E.; Hoffler, C. E.; Moore, K. E.; Goldstein, S. A. Elastic modulus and hardness of cortical and trabecular bone lamellae measured by nanoindentation in the human femur. *J. Biomech.* **1999**, *32*, 1005−1012.

DOI: 10.1021/acsbiomaterials.9b01023
ACS Biomater. Sci. Eng. 2019, 5, 5392−5411